Changes in seam number and location induce holes within microtubules assembled from porcine brain tubulin and in *Xenopus* egg cytoplasmic extracts

Charlotte Guyomar[1], Clément Bousquet[1], Siou Ku[1], John Heumann[2], Gabriel Guilloux[1], Natacha Gaillard[3], Claire Heichette[1], Laurence Duchesne[1], Michel O. Steinmetz[3,4], Romain Gibeaux[1], Denis Chrétien[1]*

[1]Univ Rennes, CNRS, IGDR (Institut de Génétique et Développement de Rennes) - UMR 6290, F-35000 Rennes, France.

[2]Department of Molecular, Cellular and Developmental Biology, University of Colorado, Boulder, CO 80309 USA.

[3]Laboratory of Biomolecular Research, Division of Biology and Chemistry, Paul Scherrer Institute, Villigen, Switzerland.

[4]University of Basel, Biozentrum, 4056 Basel, Switzerland

*Corresponding author: denis.chretien@univ-rennes1.fr

Abstract

Microtubules are tubes of about 25 nm in diameter that are critically involved in a variety of cellular functions including motility, compartmentalization, and division. They are considered as pseudo-helical polymers whose constituent αβ-tubulin heterodimers share lateral homotypic interactions, except at one unique region called the seam. Here, we used a segmented sub-tomogram averaging strategy to reassess this paradigm and analyze the organization of the αβ-tubulin heterodimers in microtubules assembled from purified porcine brain tubulin in the presence of GTP and GMPCPP, and in *Xenopus* egg cytoplasmic extracts. We find that in all conditions, microtubules incorporate variable protofilament and/or tubulin

subunit helical-start numbers, as well as variable numbers of seams. Strikingly, the seam number and location vary along individual microtubules, generating holes of one to a few subunits in size within their lattices. Together, our results reveal that the formation of mixed and discontinuous microtubule lattices is an intrinsic property of tubulin that requires the formation of unique lateral interactions without longitudinal ones. They further suggest that microtubule assembly is tightly regulated in a cytoplasmic environment.

Introduction

The organization of the αβ-tubulin heterodimer within microtubules was originally inferred from the analysis of transmission electron microscopy images of negatively stained axonemal doublets (Amos & Klug, 1974). It was proposed that the tubulin subunits engage heterotypic lateral interactions (α-β, β-α) in the complete 13 protofilaments A-microtubule, and homotypic ones (α-α, β-β) in the incomplete 10 protofilaments B-microtubule, giving rise to the concept of the A and B lattices (Figure 1A-B). However, using kinesin-motor domains that bind uniquely to β-tubulin (Figure 1C), it was shown later that in both the A and B microtubules of the doublet, tubulin heterodimers engage homotypic interactions of the B type (Song & Mandelkow, 1995), which is also the case in microtubules assembled *in vitro* from purified tubulin (Crepeau et al., 1978; Song & Mandelkow, 1993). Noticeably, for geometrical reasons (McEwen & Edelstein, 1980; Wade & Chrétien, 1993), microtubules organized with 13 protofilaments and 3-start lateral helices should contain at least one 'seam' of the A-type (Figure 1B), which corresponds to our current view of microtubule lattice organization.

Multiple seams were first visualized by freeze-etching and rotary shadowing of microtubules assembled *in vitro* (Kikkawa et al., 1994). Using the same approach on cells treated with

detergent to remove the membrane and decorate the microtubules with kinesin-motor domains, the authors provided the first evidence of a preferred B-lattice type organization *in cellulo*, and could visualize unique seams in cytoplasmic microtubules. But due to the limitation of the method and the small number of microtubules observed, they did not exclude the possibility of several seams *in cellulo*. Since then, several studies have revealed the presence of multiple seams in microtubules assembled *in vitro*, noticeably in the presence of the stabilizing drug Taxol (Debs et al., 2020; des Georges et al., 2008; Howes et al., 2017; Sosa et al., 1997). The predominance of B-type lateral contacts *in cellulo* was confirmed by cryo-electron tomography after detergent removal of the membrane and decoration with kinesin-motor domains, but with no detailed statistics (McIntosh et al., 2009). Therefore, it turns out that our knowledge on the organization of αβ-tubulin heterodimers within microtubules assembled *in vitro* in the absence of drug and *in cellulo* remains limited.

To gain a deeper understanding of microtubule lattice organization *in vitro* and in a cytoplasmic environment, we analyzed microtubules assembled from purified porcine brain tubulin in the presence of GTP, the slowly hydrolysable analogue GMPCPP, and in *Xenopus* egg cytoplasmic extracts. Microtubules were decorated with kinesin-motor domains and their binding pattern was analyzed using cryo-electron tomography followed by sub-tomogram averaging (STA). To this end, we specifically developed a segmented sub-tomogram averaging (SSTA) strategy, which allowed us to investigate the structural heterogeneity of individual microtubules. We find that in all conditions the seam number and location vary within individual microtubules, leaving holes of one to a few subunits in size within their wall. Microtubules assembled in a cytoplasmic environment are more regular, suggesting a tightly regulated process. Moreover, the formation of discontinuous mixed AB-lattices implies that tubulin can engage unique lateral interactions without longitudinal ones at the

76 growing tip, a process that accounts for the formation of holes within their wall during
77 polymerization.
78

79 ## Results

80 Microtubules were self-assembled *in vitro* from purified porcine brain tubulin in the presence
81 of 1 mM GTP (Figure 2 - figure supplement 1A) and kinesin-motor domains were added at
82 the polymerization plateau right before vitrification of the specimen grids into liquid ethane
83 (Figure 2 - figure supplement 1B). Cryo-electron tomograms were acquired preferentially
84 using a dual-axis strategy (Guesdon et al., 2013) so that all microtubules could be analyzed
85 independently of their orientation with respect to the tilt axes (Figure 2 - figure supplement
86 1C, Video 1). The low magnifications used, between 25 000 X and 29 000 X, allowed us to
87 record long stretches of the microtubules, ~1 to 2 µm in length, to optimize the sub-
88 tomographic averaging strategy along individual fibers.
89

90 ### The number and location of seams vary within individual microtubules assembled from
91 purified tubulin

92 We first processed entire microtubules present in the tomograms using a sub-tomogram
93 averaging approach that retrieves small sub-volumes of ~50 nm^3 in size at every kinesin-
94 motor domain position (Zabeo et al., 2018) (i.e., every ~8 nm; Figure 2 - figure supplement
95 2A). The resulting 3D volumes clearly revealed the protofilament number and the
96 organization of the kinesin-motor domains around the microtubule lattice (Figure 2A, Video
97 2), and hence the underlying organization of their constituent tubulin dimers (Figure 2B-C).
98 In agreement with previous studies performed on Taxol-stabilized microtubules (Debs et al.,
99 2020; des Georges et al., 2008; Howes et al., 2017; Kikkawa et al., 1994; Sosa et al., 1997),

we found that microtubules assembled *in vitro* from purified tubulin in the presence of GTP contained one to several A-lattice seams (Figure 3). However, we could frequently observe protofilaments with a much thinner appearance where the kinesin-motor domain periodicity was partly or completely lost (Figure 3A, Video 3). We hypothesized that the appearance of such aberrant protofilaments resulted from the averaging of regions containing kinesin-motor domain densities with regions falling in between. To explore this idea, we used SSTA to reconstruct short regions along individual microtubules (Figure 3B-C, Figure 3 - figure supplement 2B). Using this approach, we could identify regions where the seam number and/or location varied within individual microtubules. In the example shown in Figure 3B, the segment S1 contains 5 seams while S3 and S4 contain 3 seams. S2 still displays two aberrant protofilaments indicating that the change in seam number occurred in this region. To confirm this hypothesis, we extracted the corresponding region in the raw tomogram that was further filtered by thresholding intensities in Fourier space to increase the signal-to-noise ratio (Figure 4A). Comparison between the kinesin-motor domain patterns in the sub-tomogram averages of segments S1 to S3 with the filtered S2 region confirmed that this latter constitutes a transition zone where the seam number changes from 5 to 3. Line plots along the registered protofilaments (Figure 4B) shows that the kinesin-motor domain periodicity becomes out of phase after the transition in the aberrant protofilaments, implying an offset of at least one monomer (or an odd number) before and after the transition, and hence the presence of holes within the microtubule lattice (Figure 4C). Analysis of 24 microtubules taken on 4 tomograms, representing 195 segments of ~160 nm length (i.e., 2664 lateral interactions), revealed an average lattice type transition frequency of 3.7 μm^{-1} (Supplementary Table 1), but with a high heterogeneity. Some microtubules showed no or little lattice type transitions (e.g., MT3 and MT4, Figure 3 - figure supplementary 3A; MT16, MT21 and MT23, Figure 3 -

figure supplementary 3B), while others were heavily dislocated, with a lattice type transition frequency as high as ~15 μm^{-1} (e.g., MT13 and MT14, Figure 3 - figure supplementary 3B).

Lattice type transitions involve the formation of holes within microtubules

Direct visualization of holes within microtubules self-assembled at high tubulin concentration (40 µM) in the presence of GTP was hampered by the high background generated by free tubulin in solution. In addition, the low magnification used to analyze long stretches of the microtubules was at the detriment of resolution. To improve the quality of the raw cryo-electron tomograms, we used GMPCPP to assemble microtubules at a lower tubulin concentration (10 µM), and acquired single-axis tilt series at a magnification of 50 000 X. SSTA was performed on kinesin-motor domains decorated GMPCPP-microtubules suitably oriented with respect to the tilt axis, in order to localize transition regions and to visualize corresponding holes in their lattice. The microtubule shown in Figure 5A transitioned from 1 to 3 seams as demonstrated by SSTA. Visualization of the microtubule in the raw tomogram reveals a transition from a B- to an A-lattice organization in the 3 protofilaments located at its lower surface (Figure 3B), as assessed by the diffraction patterns of the corresponding regions, and after filtration of the equatorial and 8 nm^{-1} layer lines. Enlargement of the central region (Figure 3C) shows a hole of one subunit's size in the middle protofilament (2) that accounts for the change in lattice organization at this location. In addition, the first protofilament (1) displays a gap of one dimer's size, although we cannot exclude that this results from an absence of kinesin-motor domain. Analysis of 31 GMPCPP-microtubules taken on 6 tomograms using the same strategy as in the presence of GTP (Figure 5 - figure supplement 4) revealed a transition frequency of 1.2 μm^{-1} (Supplementary Table 1), i.e., ~3 fold lower than microtubules assembled in the presence of GTP. However, since we used different tubulin concentrations, i.e., 10 µM and 40 µM in the presence of GMPCPP and

GTP, respectively, we cannot exclude a concentration dependent effect on the lattice type transition frequency.

Methodological artefacts limit the visualization of holes within microtubules in raw cryo-electron tomograms

During this study, we found strong limitations to the observation of holes within microtubules in raw tomograms. First, the transition regions had to be located at the top or bottom surface of the microtubule with respect to the electron beam, since edges were severely smoothed due to the lack of data at high angle that elongate densities in this direction (Figure 6A-B). This artefact is inherent to electron tomography, limiting the search of holes within microtubules in raw tomograms. A second severe artefact commonly encountered, especially in thin ice layers, was denaturation of kinesin heads at the air-water interface (Figure 6C-D). This artefact shows up as a diminution of the kinesin-motor domain density, whose periodical arrangement can only be recovered after SSTA (Figure 6D). This analysis clearly showed that SSTA remains compulsory to localize changes in lattice type organization within individual microtubules, and thus visualize the corresponding holes in regions suitably oriented with respect to the tilt axis and not in interaction with the air-water interfaces.

Lattice type transitions occur in a cytoplasmic environment

Next, we wondered whether the formation of holes was an intrinsic property of tubulin polymerization and if such microtubule lattice defects were also present in a cellular context. Decorating microtubules with kinesin-motor domains in cells remains challenging, since it involves removing of the cell membrane with detergents, adding kinesin-motor domains, and obtaining specimens thin enough to be analyzed by electron microscopy (Kikkawa et al.,

1994; McIntosh et al., 2009). To overcome these difficulties and allow the analysis of a large data set of cytoplasmic microtubules, we took advantage of the open cellular system constituted by metaphase-arrested *Xenopus* egg cytoplasmic extracts (Gibeaux & Heald, 2019). Microtubule assembly was triggered using either DMSO (Sawin & Mitchison, 1994) or a constitutively active form of Ran (RanQ69L, (Carazo-Salas et al., 1999)) to control for possible effects of DMSO. Cryo-fluorescence microscopy was initially used to optimize the density of microtubule asters onto electron-microscope grids (Figure 7A). For structural analysis, kinesin-motor domains were added to fluorescent label-free cytoplasmic extracts right before vitrification (Figure 7 - figure supplement 1D), and specimens were imaged using dual-axis cryo-electron tomography (Figure 7B, Video 4) followed by SSTA.

The vast majority of the microtubule segments were organized according to 13 protofilaments, three-start helices in a B-lattice configuration with one single seam (Figure 8 - figure supplement 5, Supplementary Table 2). Yet, lattice type transitions were observed in six cases over the 64 microtubules analyzed in the DMSO sample (Figure 8 - figure supplement 5, MT2, MT5, MT14, MT18, MT28, MT56). Similarly, 2 lattice type transitions were observed over 15 microtubules analyzed in the Ran sample (Figure 8 - figure supplement 6, MT4, MT10), showing that the presence of transitions was independent of the method used to trigger microtubule aster formation. The transition lattice type frequencies were ~0.1 μm^{-1} (Supplementary Table 1), i.e., at least one order of magnitude less than with microtubules assembled from purified tubulin in the presence of GMPCPP and GTP, respectively. Strikingly, these transitions systematically involved a lateral offset of the seam by one protofilament (Figure 8, Video 5). In addition, variations in protofilament and helix-start numbers were also observed such as 12_2, 12_3, 13_4 and 14_3 microtubule-lattice regions (Figure 9). Of note, the 12_2 and 13_4 microtubules showed a local dislocation in

198 between two protofilaments (Video 6), which is likely a response to the excessive
199 protofilament skewing present in these microtubules (Chrétien & Fuller, 2000). The 12_2
200 microtubule contained two seams (Figure 9A), while the 13_4 microtubules had no seam
201 (Figure 9C), and hence were fully helical at the tubulin dimer level (MT7 and MT8, Figure 9 -
202 figure supplement 5A). These observations demonstrate that changes in protofilament and/or
203 helix-start numbers, as well as multiple seams and transitions in lattice types, occur within
204 individual microtubules assembled in a cytoplasmic context.
205

206 ## Discussion

207 Here we used a segmented sub-tomogram strategy to reveal changes in lattice types within
208 individual microtubules assembled from purified tubulin or in a cytoplasmic context, and
209 hence holes within their lattice. Ideally, cryo-electron tomography should reveal holes in the
210 absence of averaging. Yet, we found severe limitations that are independent of the instrument
211 used, but that are linked to the methodology. First, missing data at high angle, whether they
212 are taken by single- or dual-axis cryo-electron tomography, blur densities on the edges of
213 microtubules with respect to the tilt axis (Guesdon et al., 2013). Second, we found that the
214 interaction of the microtubules with the air-water interface diminishes the kinesin-motor
215 domain densities, likely as a consequence of denaturation (D'Imprima et al., 2019; Klebl et
216 al., 2022). Third, the lattice type transition frequency remains low with respect to the number
217 of tubulin heterodimers within microtubules. It is 3.7 and 1.2 transitions every µm for
218 microtubules assembled in the presence of GTP, and GMPCPP, respectively, and ~1 every
219 ~10 µm for cytoplasmic extract microtubules. Considering that 1 µm of a 13 protofilament
220 microtubule contains ~1 625 dimers, this translates to one lattice type transition every 16 250
221 dimers, which hinders the localization of holes in raw data. Conversely, the original SSTA
222 approach we used allows localization of lattice type transitions along individual microtubules

223 independently of their orientation with respect to the tilt axis, and at surfaces that interact with
224 the air-water interface. While missing data at high angle are inherent to the method of electron
225 tomography, means to limit denaturation of proteins at the air-water interface must be found.
226 This is critical for cryo-electron tomography, but also for single particle analysis methods
227 where this artefact is a limiting factor to obtain high-resolution data (J. Chen et al., 2019; S.
228 Chen et al., 2022; D'Imprima et al., 2019; Klebl et al., 2022; Li et al., 2021).

229

230 Changes in lattice types along individual microtubules could result from an imperfect
231 annealing of shorter microtubules, a process known to occur *in vitro* (Rothwell et al., 1986).
232 Yet, the lattice type transition frequency observed with purified tubulin would necessitate
233 annealing of very short segments, sometime a few tens to hundreds of nm in length. The
234 average lattice type transition frequency observed in cytoplasmic extracts could be compatible
235 with annealing of microtubules a few µm in length. However, the fact that these transitions
236 involved systematically a lateral seam offset of only one protofilament suggests a firm
237 regulatory mechanism. Hence, a more plausible explanation is that these lattice discontinuities
238 are formed during microtubule assembly (Figure 10, Video 7). At present, classical models of
239 microtubule elongation hypothesize that tubulin engages either uniquely longitudinal
240 interactions (Figure 10A, step 1), or both longitudinal and lateral interactions with the
241 growing tip of microtubules (Figure 10B, step 2). A purely longitudinal elongation process
242 (McIntosh et al., 2018) can hardly explain how microtubules can vary in terms of
243 protofilament and/or helix start numbers as well as in lattice types, and thus how holes can
244 arise during assembly. Conversely, to account for the presence of holes of one to a few
245 subunits in size, it is sufficient to consider that tubulin can engage lateral interactions without
246 longitudinal ones (Figure 10A, step 3). Gaps of an odd number of tubulin subunits will induce
247 lattice type transitions (Figure 10A, steps 4-5), while those of an even number will induce no

changes (Figure 10B). Hence, since both types of events are likely to occur, we may underestimate the presence of holes within microtubules. In addition, a finer sampling of the microtubule lattice with shorter segments could also reveal a higher hole frequency. Formation of lateral contacts without longitudinal ones at the seam region can also explain how the seam can vary in position by one protofilament (Figure 10C), since this only requires that a tubulin dimer engages homotypic lateral interactions at the seam region (Figure 10C, step 2). This event will also leave a gap of an odd number of subunits within the microtubule lattice (Figure 10C, steps 3-4).

Our current view of microtubules organized according to a perfect pseudo-helical B-lattice interrupted by a single A-lattice seam must be reconsidered. This is definitely the case for microtubules assembled from purified tubulin and has profound consequences for the interpretation of biochemical, biophysical, and structural results. For instance, 3D reconstruction studies will have to take into account the heterogeneity of the microtubule lattice to reach higher resolution (Debs et al., 2020). The lattice organization of cytoplasmic extract microtubules is more in agreement with the B-lattice, single seam model. However, exceptions are also observed such as changes in protofilament and/or helix start numbers, as well as in the location of seams within individual microtubules. Therefore, our results suggest that the formation of heterogeneous microtubule lattices is an intrinsic property of tubulin polymerization, which is firmly regulated in cells. One key regulatory factor could be the γ-tubulin ring complex (γTuRC), which imposes the 13 protofilament organization to a nascent microtubule (Böhler et al., 2021). But how this structure is preserved during microtubule elongation remains unclear, especially if one considers a two-dimensional assembly process where the lattice can vary in terms of protofilament number, helix-start number, or lattice type during elongation. Proteins of the end-binding (EB) family are other good candidates that

could play a key role in regulating microtubule structure during assembly in cells. They interact with the tip of growing microtubules and bind in between protofilaments that are organized according to a B-lattice (Maurer et al., 2012); they thus may favor the formation of homotypic lateral interactions during assembly. In addition, EBs have been shown to induce the formation of 13 protofilaments, three-start helix microtubules (Manka & Moores, 2018; Vitre et al., 2008), which could also be forced to adopt a preferential B-lattice type organization. Conversely, microtubule polymerases like XMAP215, which act at growing microtubule ends (Brouhard et al., 2008), may favor lattice heterogeneities (Farmer et al., 2021). It remains to be determined whether the concerted action of different microtubule growing-end binding proteins regulate microtubule structure and dynamics in cells (Akhmanova & Steinmetz, 2008).

Ideas and speculation

Microtubules alternate stochastically between growing and shrinking states, an unusual behavior termed dynamic instability that was discovered some 38 years ago (Mitchison & Kirschner, 1984). Although it is exquisitely regulated in cells by a myriad of microtubule associated proteins (Cleary & Hancock, 2021), it is also an intrinsic property of microtubules assembled from purified tubulin, demonstrating that it is intimately tied to tubulin assembly properties (Brouhard, 2015).

The αβ-tubulin heterodimer binds two molecules of GTP, one located between the α and β monomers at the non-exchangeable N-site, and one on the β-subunit at the longitudinal interface between heterodimers at the E-site that becomes hydrolyzed to GDP during assembly. GTP-hydrolysis destabilizes the microtubule lattice, likely weakening tubulin lateral interactions by a mechanism that remains unclear (Zhang et al., 2015). A slight delay

between polymerization and GTP-hydrolysis would allow the formation of a protective GTP-cap at growing microtubule ends (Pantaloni & Carlier, 1986). The current model(s) speculate that stochastic loss of this GTP-cap induces depolymerization events known as catastrophes (Mitchison & Kirschner, 1984). However, the molecular mechanisms that lead to disappearance of the GTP-cap remain unknown. The origin of repolymerization events, termed rescues, is also unclear, but may involve tubulin molecules that have not hydrolyzed their GTP and that remain trapped inside the microtubule lattice (Dimitrov et al., 2008). Noteworthy, the vast majority of theoretical models that have been designed so far to explain microtubule dynamic instability rely on a continuous lattice composed of B-type lattice contacts interrupted by a single seam of the A-type (Bowne-Anderson et al., 2013, 2015). Yet, exceptions to this rule have been documented over the years, essentially in microtubules assembled *in vitro* from purified tubulin. It is known that microtubules can accommodate different protofilament and helix-start numbers (Chaaban & Brouhard, 2017; Chrétien & Wade, 1991). These numbers can vary within individual microtubules (Chrétien et al., 1992), necessarily leaving holes inside their lattice (Schaedel et al., 2019; Théry & Blanchoin, 2021). Microtubules can also adopt configurations with a high protofilament skew that must be compensated by a relaxation step whose detailed mechanism remains to be described (Chrétien & Fuller, 2000). Microtubules with different numbers of seams have been described (Debs et al., 2020; des Georges et al., 2008; Howes et al., 2017; Kikkawa et al., 1994; Sosa et al., 1997), although it was not considered that both the seam number and location could vary within individual microtubules. Therefore, these previous studies and the present one indicate that the microtubule lattice is highly labile, with the ability to form different kinds of structural defects (Hunyadi et al., 2005; Rai et al., 2021).

The formation of lattice defects during microtubule polymerization must impose energetical penalties at the growing microtubule end, potentially destabilizing the protective GTP-cap if present, and hence be at the origin of catastrophes. Likewise, holes must let patches of unhydrolyzed GTP-tubulin molecules within microtubules, potentially at the origin of rescues. Hence, we propose that microtubule dynamic instability is not only driven by the nucleotide state of tubulin, but also by the intrinsic structural instability of the microtubule lattice. MAPs such as EBs and XMAP215 may exploit this structural instability to finely tune microtubule dynamics in cells.

Materials and Methods

Protein purification

Tubulin was isolated from porcine brain by two cycles of assembly disassembly (Castoldi & Popov, 2003), followed by a final cycle in the absence of free GTP (Ashford & Hyman, 2006). Tubulin was obtained in BRB80 (80 mM K-Pipes, 1 mM EGTA, 1 mM $MgCl_2$, pH 6.8 with KOH) and stored at -80 °C before use.

The cDNA fragment encoding for the human Kif5B motor domain (residues 1 to 349) was cloned into the pET based bacterial vector PSTCm1 (Olieric et al., 2010). The protein was expressed in Rosetta2 *E. coli* cells. Cells were grown at 37 °C in LB media supplemented with 50 µg/ml kanamycin and 30 µg/ml chloramphenicol to an OD_{600} of 0.4 to 0.6. Temperature was reduced to 20 °C, the protein production was induced 20 min later with 0.5 mM IPTG (isopropy-1-thio-β-galactopyranoside), and incubation was continued overnight under agitation. The cells were harvested by centrifugation for 15 min at 4 000 *g* and the cell pellets were resuspended in lysis buffer (50 mM HEPES, pH 8.0, supplemented with 10 mM imidazole, 10 % glycerol, 0.1 mM ADP, 2 mM beta-mercaptoethanol, and one cOmplete

EDTA free proteases inhibitor cocktail tablet per 50 mL buffer). The cells were lysed on ice per ultrasonication and lysate clearing was performed by centrifugation, 30 min at 24 000 *g*. The resultant supernatant was filtered using a 0.45 µm filter and the protein was subsequently purified by IMAC on a 5 ml HP HisTrap column (GE Healthcare) according to manufacturer's information. The eluted protein from this affinity step was concentrated and further purified by gel filtration on a HiLoad® 16/600 Superdex® 200 pg column (GE Healthcare) equilibrated in 20 mM TrisHCl, pH 7.5, supplemented with 150 mM NaCl, 0.1 mM ADP, and 2 mM DTT. The homogeneity of the recombinant Kif5B motor domain was assessed by SDS-PAGE. Fractions were concentrated, aliquoted, flash frozen into liquid nitrogen, and stored at -80 °C.

Animals

All animal experimentation in this study was performed according to our animal use protocol APAFiS #26858-2020072110205978 approved by the Animal Use Ethic Committee (#7, Rennes, France) and the French Ministry of Higher Education, Research and Innovation. Mature *Xenopus laevis* female frogs were obtained from the CRB Xénope (Rennes, France) and ovulated with no harm to the animals with at least a 6-month rest interval between ovulations.

***Xenopus* egg cytoplasmic extracts**

Cytostatic factor-arrested (CSF) egg extracts were prepared from freshly laid eggs of *Xenopus laevis* as previously described (Good & Heald, 2018; Murray, 1991). Briefly, eggs arrested in metaphase of meiosis II were collected, dejellied and fractionated by centrifugation. The cytoplasmic layer was isolated, supplemented with 10 mg/ml each of the protease inhibitors leupeptin, pepstatin and chymostatin (LPC), 20 mM cytochalasin B, and a creatine phosphate

and ATP energy regeneration mix. Vitrification of the samples for cryo-electron microscopy was performed the same day as the egg extract preparation.

Cryo-fluorescence microscopy

To determine the optimal density of microtubule structures assembled from *Xenopus* egg cytoplasmic extracts cryo-fixed on electron microscopy grids suitable for cryo-electron tomography acquisitions, we used cryo-fluorescence microscopy. Egg extracts were supplemented with 40 ng/µg rhodamine-tubulin before microtubule assembly was conducted by addition of 5% DMSO and incubation at 23 °C, for 30 to 45 min. Reactions were then extemporaneously diluted 1:10, 1:50 or 1:100 in 1X BRB80 buffer for vitrification on an electron microscopy grid. Frozen grids were imaged within a Linkam CMS196M cryo-correlative microscopy stage mounted on an Olympus BX51 microscope equipped with a Lumencor SOLA SE U-nIR light source, UPLFLN10X/0.30 and LMPLFLN50X/0.50 objectives, and a Photometrics Prime-BSI sCMOS Back Illuminated camera. Images were acquired using the µManager acquisition software v1.4 (Edelstein et al., 2014).

Cryo-electron tomography

Microtubules were assembled from purified porcine brain tubulin at 40 µM in BRB80, 1 mM GTP, or at 10 µM in BRB80, 0.1 mM GMPCPP, for about 1 h. Kif5B was diluted at a final concentration of 2.5 mg/ml in BRB80, 0.1 mM ATP, 1 mM GTP and 60 nM mix-matrix capped gold nanoparticles (Duchesne et al., 2008; Guesdon et al., 2016) and pre-warmed at 35 °C. First, 3 µl of the microtubule sample was deposited at the surface of a glow-discharged holey carbon grid (Quantifoil R2/2, Cu200) in the temperature (35 °C) and humidity-controlled atmosphere (~95 %) of an automatic plunge-freezer (EM-GP, Leica). Then, 3 µl of the pre-warmed kinesin motor domain suspension was added to the grid onto the sample,

incubated for 30 s, and blotted manually. An additional 3 µl of the pre-warmed kinesin motor domain suspension was added to the grid, blotted with the EMGP for 2 s using Whatman grade 1 filter paper and plunged into liquid ethane.

Microtubule aster assembly was induced in *Xenopus* egg cytoplasmic extracts by adding 5% DMSO or 15 µM of the GTPase deficient Ran mutant RanQ69L purified as previously described (Helmke & Heald, 2014), and incubating at 23 °C for 30 to 45 min. Kif5B was diluted at a final concentration of 2.5 mg/ml in BRB80, 0.1 mM ATP, 1 mM GTP and 60 nM mix-matrix capped gold nanoparticles (Duchesne et al., 2008; Guesdon et al., 2016), and pre-warmed at 23 °C. A 3 µl volume of the Kif5B suspension was first deposited at the surface of a glow-discharged holey carbon grid (Quantifoil R2/2, Cu200) in the temperature (23 °C) and humidity-controlled atmosphere (~95 %) of the EM-GP, on the side of the grid to be blotted. Right away, one volume of the extract sample was diluted 50 X in the pre-warmed Kif5B suspension, and 3 µl of this mix was deposited on the other side of the grid. The grid was blotted from the opposite side of the sample with the EM-GP for 4 s using Whatman grade filter 4 and plunged into liquid ethane.

For dual-axis cryo-electron tomography, specimen grids were transferred to a rotating cryo-holder (model CT3500TR, Gatan), and observed using a 200 kV electron microscope equipped with a LaB_6 cathode (Tecnai G^2 T20 Sphera, FEI). Images of microtubules assembled from purified tubulin were recorded on a 4k x 4K CCD camera (USC4000, Gatan) in binning mode 2 and at a nominal magnification of 29 000 X, providing a final pixel size of 0.79 nm. Images of microtubules assembled in *Xenopus* egg extracts were recorded on a 4K x 4k CMOS camera (XF416, TVIPS) in binning mode 2 and at a nominal magnification of 25 000 X and 29 000 X, providing final pixel sizes of 0.87 nm and 0.74 nm, respectively. Pixel

422 sizes were calibrated using TMV as a standard (Guesdon et al., 2016). Dual-axis cryo-electron
423 tomography data were acquired as previously described (Guesdon et al., 2013). Briefly, a first
424 tilt series of ~40 images was taken in an angular range of ~±60° starting from 0° and using a
425 Saxton scheme. The specimen was turned by a ~90° in plane rotation at low magnification
426 and a second tilt series was taken on the same area using parameters identical to the first
427 series. Tomograms were reconstructed using the Etomo graphical user interface of the IMOD
428 program (Kremer et al., 1996; Mastronarde, 1997). Tilt series were typically filtered after
429 alignment using a low pass filter at 0.15 cycles/pixels and a sigma of 0.05. Tomograms were
430 reconstructed in 3D using the SIRT-like filter of Etomo with 15 equivalent iterations. Dual-
431 axis cryo-electron tomograms were converted to bytes before further processing.
432
433 For single-axis cryo-electron tomography, specimen grids were transferred to a dual grid
434 cryo-transfer holder model 205 (Simple Origin). Data were acquired on a 4K x 4k CMOS
435 camera (XF416, TVIPS) in binning mode 1 and at a nominal magnification of 50 000 X,
436 providing a final pixel size of 0.21 nm. Typically, 40 images were taken in an angular range
437 of ~±60° starting from 0°, or using a symmetric electron dose scheme (Hagen et al., 2017). To
438 localize holes within microtubules by SSTA, tomograms were subsequently binned by 4 to
439 provide a final pixel size of 0.83 nm.
440
441 **Sub-tomogram averaging**
442 Sub-tomogram averages were calculated using the procedure described online
443 (https://bio3d.colorado.edu/RML_2017/2017_IMOD_PEET_Workshop/Lab_Instructions/L8
444 Microtubules.pdf). Briefly, a first model was created by following individual protofilaments
445 in cross section using the slicer tool in IMOD. Usually, ~50 electronic slices were averaged to
446 reinforce the contrast. A second model was next extrapolated from the first one to mark the

447 microtubule center at the same point positions. Then, a third model was calculated from the
448 previous ones with points spaced every ~8 nm, and a motive list containing Euler angles of
449 each sub-volume with respect to the chosen reference was created. Sub-volumes of ~40
450 pixels^3 were extracted at each point position using the graphical user interface of the PEET
451 program (Nicastro et al., 2006). Registration of the microtubule segments was performed by
452 cross-correlation, limiting rotational angular searches around the microtubule axis to about
453 half the angular separation between protofilaments. Other angles were set to take into account
454 variations of microtubule curvature in the X, Y and Z directions. Segmented sub-tomogram
455 averaging was performed using a new routine (splitIntoNsegments) implemented into the
456 PEET program version 1.14.1. This routine splits the initial model and motive list into *N*
457 segments of equal size and creates sub-directories for each segment. Sub-tomogram averages
458 are calculated for each segment, using the original sub-tomogram average parameters of the
459 whole microtubule as a template.
460
461 **Image analysis and model building**
462 Sub-tomogram averages were inspected using the isosurface panel of IMOD. Four scattered
463 models were created. Model 1 was used to mark the kinesin motor domain densities (yellow
464 spheres), model 2 to mark the absence of densities (cyan spheres), model 3 aberrant densities
465 (red spheres), and model 4 the microtubule center. Spheres from model 1 to 3 were placed
466 along the *S*-start lateral helices. The 4th last model was enlarged to cross the kinesin motor
467 domain densities in order to place the other spheres at a same radius. The number of
468 protofilaments and the different lateral contacts (A, B and undefined lateral contacts) were
469 retrieved from these models.
470
471

Acknowledgments

Cryo-electron microscopy data were acquired on the Microscopy Rennes imaging center platform (Biosit, Rennes, France), member of the national infrastructure France-BioImaging (FBI) supported by the French National Research Agency (ANR-10-INBS-04). *Xenopus laevis* eggs were obtained from the Centre de Ressources Biologique Xénopes, Université de Rennes 1, Rennes, France. Porcine brains were kindly provided by Y. Drillet, Cooperl Arc Altantique, Lamballe France. Tobacco Mosaic Virus was kindly provided by T. Candresse, UMR 13332 Biologie du Fruit et Pathologie, INRAE and University of Bordeaux, Villenave d'Ornon, France. Video 7 was designed by A. Kawska, Illuscienta, Paris, France. This work was supported by two French National Research Agency grants (ANR-16-CE11-0017-01 to D.C. and M.O.S., and ANR-18-CE13-0001-01 to D.C.), a Swiss National Science Foundation grant (310030_192566 to M.O.S.) and a Human Frontier Science Program grant (CDA00019/2019-C to R.G.).

References

Akhmanova, A., & Steinmetz, M. O. (2008). Tracking the ends□: A dynamic protein network controls the fate of microtubule tips. *Nature Reviews. Molecular Cell Biology*, *9*(4), 309□322. https://doi.org/10.1038/nrm2369

Amos, L. A., & Klug, A. (1974). Arrangement of subunits in flagellar microtubules. *Journal of Cell Science*, *14*(3), 523□549 https://doi.org/10.1242/jcs.14.3.523

Ashford, A. J., & Hyman, A. A. (2006). Chapter 22—Preparation of Tubulin from Porcine Brain. In J. E. Celis (Éd.), *Cell Biology (Third Edition)* (p. 155□160). Academic Press. https://doi.org/10.1016/B978-012164730-8/50094-0

Böhler, A., Vermeulen, B. J. A., Würtz, M., Zupa, E., Pfeffer, S., & Schiebel, E. (2021). The gamma-tubulin ring complex□: Deciphering the molecular organization and assembly

497 mechanism of a major vertebrate microtubule nucleator. *BioEssays*, *43*(8), 2100114.
498 https://doi.org/10.1002/bies.202100114
499 Bowne-Anderson, H., Hibbel, A., & Howard, J. (2015). Regulation of Microtubule Growth
500 and Catastrophe : Unifying Theory and Experiment. *Trends in cell biology*, *25*(12),
501 769 779. https://doi.org/10.1016/j.tcb.2015.08.009
502 Bowne-Anderson, H., Zanic, M., Kauer, M., & Howard, J. (2013). Microtubule dynamic
503 instability : A new model with coupled GTP hydrolysis and multistep catastrophe.
504 *BioEssays: News and Reviews in Molecular, Cellular and Developmental Biology*, *35*(5),
505 452 461. https://doi.org/10.1002/bies.201200131
506 Brouhard, G. J. (2015). Dynamic instability 30 years later : Complexities in microtubule
507 growth and catastrophe. *Molecular Biology of the Cell*, *26*(7), 1207 1210.
508 https://doi.org/10.1091/mbc.E13-10-0594
509 Brouhard, G. J., Stear, J. H., Noetzel, T. L., Al-Bassam, J., Kinoshita, K., Harrison, S. C.,
510 Howard, J., & Hyman, A. A. (2008). XMAP215 is a processive microtubule polymerase.
511 *Cell*, *132*(1), 79 88. https://doi.org/10.1016/j.cell.2007.11.043
512 Carazo-Salas, R. E., Guarguaglini, G., Gruss, O. J., Segref, A., Karsenti, E., & Mattaj, I. W.
513 (1999). Generation of GTP-bound Ran by RCC1 is required for chromatin-induced mitotic
514 spindle formation. *Nature*, *400*(6740), 178 181. https://doi.org/10.1038/22133
515 Castoldi, M., & Popov, A. V. (2003). Purification of brain tubulin through two cycles of
516 polymerization–depolymerization in a high-molarity buffer. *Protein Expression and*
517 *Purification*, *32*(1), 83 88. https://doi.org/10.1016/S1046-5928(03)00218-3
518 Chaaban, S., & Brouhard, G. J. (2017). A microtubule bestiary : Structural diversity in
519 tubulin polymers. *Molecular Biology of the Cell*, *28*(22), 2924 2931.
520 https://doi.org/10.1091/mbc.E16-05-0271
521 Chen, J., Noble, A. J., Kang, J. Y., & Darst, S. A. (2019). Eliminating effects of particle

522 adsorption to the air/water interface in single-particle cryo-electron microscopy□: Bacterial
523 RNA polymerase and CHAPSO. *Journal of Structural Biology: X*, *1*, 100005.
524 https://doi.org/10.1016/j.yjsbx.2019.100005
525 Chen, S., Li, J., Vinothkumar, K. R., & Henderson, R. (2022). Interaction of human
526 erythrocyte catalase with air–water interface in cryoEM. *Microscopy*, *71*(Supplement_1),
527 i51□i59. https://doi.org/10.1093/jmicro/dfab037
528 Chrétien, D., & Fuller, S. D. (2000). Microtubules switch occasionally into unfavorable
529 configurations during elongation. *Journal of Molecular Biology*, *298*(4), 663□676.
530 https://doi.org/10.1006/jmbi.2000.3696
531 Chrétien, D., Metoz, F., Verde, F., Karsenti, E., & Wade, R. (1992). Lattice defects in
532 microtubules□: Protofilament numbers vary within individual microtubules. *Journal of Cell*
533 *Biology*, *117*(5), 1031□1040. https://doi.org/10.1083/jcb.117.5.1031
534 Chrétien, D., & Wade, R. H. (1991). New data on the microtubule surface lattice. *Biology of*
535 *the Cell*, *71*(1□2), 161□174. https://doi.org/10.1016/0248-4900(91)90062-r
536 Cleary, J. M., & Hancock, W. O. (2021). Molecular mechanisms underlying microtubule
537 growth dynamics. *Current Biology: CB*, *31*(10), R560□R573.
538 https://doi.org/10.1016/j.cub.2021.02.035
539 Crepeau, R. H., McEwen, B., & Edelstein, S. J. (1978). Differences in alpha and beta
540 polypeptide chains of tubulin resolved by electron microscopy with image reconstruction.
541 *Proceedings of the National Academy of Sciences of the United States of America*, *75*(10),
542 5006□5010. https://doi.org/10.1073/pnas.75.10.5006
543 Debs, G. E., Cha, M., Liu, X., Huehn, A. R., & Sindelar, C. V. (2020). Dynamic and
544 asymmetric fluctuations in the microtubule wall captured by high-resolution cryoelectron
545 microscopy. *Proceedings of the National Academy of Sciences of the United States of*
546 *America*, *117*(29), 16976□16984. https://doi.org/10.1073/pnas.2001546117

des Georges, A., Katsuki, M., Drummond, D. R., Osei, M., Cross, R. A., & Amos, L. A. (2008). Mal3, the Schizosaccharomyces pombe homolog of EB1, changes the microtubule lattice. *Nature Structural & Molecular Biology*, *15*(10), 1102–1108. https://doi.org/10.1038/nsmb.1482

Dimitrov, A., Quesnoit, M., Moutel, S., Cantaloube, I., Poüs, C., & Perez, F. (2008). Detection of GTP-tubulin conformation in vivo reveals a role for GTP remnants in microtubule rescues. *Science (New York, N.Y.)*, *322*(5906), 1353–1356. https://doi.org/10.1126/science.1165401

D'Imprima, E., Floris, D., Joppe, M., Sánchez, R., Grininger, M., & Kühlbrandt, W. (2019). Protein denaturation at the air-water interface and how to prevent it. *eLife*, *8*, e42747. https://doi.org/10.7554/eLife.42747

Duchesne, L., Gentili, D., Comes-Franchini, M., & Fernig, D. G. (2008). Robust Ligand Shells for Biological Applications of Gold Nanoparticles. *Langmuir*, *24*(23), 13572–13580. https://doi.org/10.1021/la802876u

Edelstein, A. D., Tsuchida, M. A., Amodaj, N., Pinkard, H., Vale, R. D., & Stuurman, N. (2014). Advanced methods of microscope control using μManager software. *Journal of Biological Methods*, *1*(2), e10–e10. https://doi.org/10.14440/jbm.2014.36

Farmer, V., Arpağ, G., Hall, S. L., & Zanic, M. (2021). XMAP215 promotes microtubule catastrophe by disrupting the growing microtubule end. *Journal of Cell Biology*, *220*(10), e202012144. https://doi.org/10.1083/jcb.202012144

Gibeaux, R., & Heald, R. (2019). The Use of Cell-Free Xenopus Extracts to Investigate Cytoplasmic Events. *Cold Spring Harbor Protocols*, *2019*(6). https://doi.org/10.1101/pdb.top097048

Good, M. C., & Heald, R. (2018). Preparation of Cellular Extracts from Xenopus Eggs and Embryos. *Cold Spring Harbor Protocols*, *2018*(6), pdb.prot097055.

https://doi.org/10.1101/pdb.prot097055

Guesdon, A., Bazile, F., Buey, R. M., Mohan, R., Monier, S., García, R. R., Angevin, M., Heichette, C., Wieneke, R., Tampé, R., Duchesne, L., Akhmanova, A., Steinmetz, M. O., & Chrétien, D. (2016). EB1 interacts with outwardly curved and straight regions of the microtubule lattice. *Nature Cell Biology*, *18*(10), 1102–1108. https://doi.org/10.1038/ncb3412

Guesdon, A., Blestel, S., Kervrann, C., & Chrétien, D. (2013). Single versus dual-axis cryo-electron tomography of microtubules assembled in vitro: Limits and perspectives. *Journal of Structural Biology*, *181*(2), 169–178. https://doi.org/10.1016/j.jsb.2012.11.004

Hagen, W. J. H., Wan, W., & Briggs, J. A. G. (2017). Implementation of a cryo-electron tomography tilt-scheme optimized for high resolution subtomogram averaging. *Journal of Structural Biology*, *197*(2), 191–198. https://doi.org/10.1016/j.jsb.2016.06.007

Helmke, K. J., & Heald, R. (2014). TPX2 levels modulate meiotic spindle size and architecture in Xenopus egg extracts. *The Journal of Cell Biology*, *206*(3), 385–393. https://doi.org/10.1083/jcb.201401014

Howes, S. C., Geyer, E. A., LaFrance, B., Zhang, R., Kellogg, E. H., Westermann, S., Rice, L. M., & Nogales, E. (2017). Structural differences between yeast and mammalian microtubules revealed by cryo-EM. *The Journal of Cell Biology*, *216*(9), 2669–2677. https://doi.org/10.1083/jcb.201612195

Hunyadi, V., Chrétien, D., & Jánosi, I. M. (2005). Mechanical stress induced mechanism of microtubule catastrophes. *Journal of Molecular Biology*, *348*(4), 927–938. https://doi.org/10.1016/j.jmb.2005.03.019

Kikkawa, M., Ishikawa, T., Nakata, T., Wakabayashi, T., & Hirokawa, N. (1994). Direct visualization of the microtubule lattice seam both in vitro and in vivo. *The Journal of Cell Biology*, *127*(6 Pt 2), 1965–1971. https://doi.org/10.1083/jcb.127.6.1965

Klebl, D. P., Wang, Y., Sobott, F., Thompson, R. F., & Muench, S. P. (2022). It started with a Cys□: Spontaneous cysteine modification during cryo-EM grid preparation. *Frontiers in Molecular Biosciences*, *9*. https://www.frontiersin.org/articles/10.3389/fmolb.2022.945772

Kremer, J. R., Mastronarde, D. N., & McIntosh, J. R. (1996). Computer Visualization of Three-Dimensional Image Data Using IMOD. *Journal of Structural Biology*, *116*(1), 71□76. https://doi.org/10.1006/jsbi.1996.0013

Li, B., Zhu, D., Shi, H., & Zhang, X. (2021). Effect of charge on protein preferred orientation at the air–water interface in cryo-electron microscopy. *Journal of Structural Biology*, *213*(4), 107783. https://doi.org/10.1016/j.jsb.2021.107783

Manka, S. W., & Moores, C. A. (2018). Microtubule structure by cryo-EM□: Snapshots of dynamic instability. *Essays in Biochemistry*, *62*(6), 737□751. https://doi.org/10.1042/EBC20180031

Mastronarde, D. N. (1997). Dual-Axis Tomography□: An Approach with Alignment Methods That Preserve Resolution. *Journal of Structural Biology*, *120*(3), 343□352. https://doi.org/10.1006/jsbi.1997.3919

Maurer, S. P., Fourniol, F. J., Bohner, G., Moores, C. A., & Surrey, T. (2012). EBs recognize a nucleotide-dependent structural cap at growing microtubule ends. *Cell*, *149*(2), 371□382. https://doi.org/10.1016/j.cell.2012.02.049

McEwen, B., & Edelstein, S. J. (1980). Evidence for a mixed lattice in microtubules reassembled in vitro. *Journal of Molecular Biology*, *139*(2), 123□143. https://doi.org/10.1016/0022-2836(80)90300-9

McIntosh, J. R., Morphew, M. K., Grissom, P. M., Gilbert, S. P., & Hoenger, A. (2009). Lattice structure of cytoplasmic microtubules in a cultured Mammalian cell. *Journal of Molecular Biology*, *394*(2), 177□182. https://doi.org/10.1016/j.jmb.2009.09.033

McIntosh, J. R., O'Toole, E., Morgan, G., Austin, J., Ulyanov, E., Ataullakhanov, F., &

622 Gudimchuk, N. (2018). Microtubules grow by the addition of bent guanosine triphosphate
623 tubulin to the tips of curved protofilaments. *Journal of Cell Biology*, *217*(8), 2691□2708.
624 https://doi.org/10.1083/jcb.201802138
625 Mitchison, T., & Kirschner, M. (1984). Dynamic instability of microtubule growth. *Nature*,
626 *312*(5991), 237□242. https://doi.org/10.1038/312237a0
627 Murray, A. W. (1991). Cell cycle extracts. *Methods in Cell Biology*, *36*, 581□605.
628 Nicastro, D., Schwartz, C., Pierson, J., Gaudette, R., Porter, M. E., & McIntosh, J. R. (2006).
629 The Molecular Architecture of Axonemes Revealed by Cryoelectron Tomography. *Science*,
630 *313*(5789), 944□948. https://doi.org/10.1126/science.1128618
631 Olieric, N., Kuchen, M., Wagen, S., Sauter, M., Crone, S., Edmondson, S., Frey, D.,
632 Ostermeier, C., Steinmetz, M. O., & Jaussi, R. (2010). Automated seamless DNA co-
633 transformation cloning with direct expression vectors applying positive or negative insert
634 selection. *BMC Biotechnology*, *10*(1), 56. https://doi.org/10.1186/1472-6750-10-56
635 Pantaloni, D., & Carlier, M.-F. (1986). Involvement of Guanosine Triphosphate (GTP)
636 Hydrolysis in the Mechanism of Tubulin Polymerization□: Regulation of Microtubule
637 Dynamics at Steady State by a GTP Cap. *Annals of the New York Academy of Sciences*,
638 *466*(1), 496□509. https://doi.org/10.1111/j.1749-6632.1986.tb38427.x
639 Rai, A., Liu, T., Katrukha, E. A., Estévez-Gallego, J., Manka, S. W., Paterson, I., Díaz, J. F.,
640 Kapitein, L. C., Moores, C. A., & Akhmanova, A. (2021). Lattice defects induced by
641 microtubule-stabilizing agents exert a long-range effect on microtubule growth by promoting
642 catastrophes. *Proceedings of the National Academy of Sciences*, *118*(51), e2112261118.
643 https://doi.org/10.1073/pnas.2112261118
644 Rothwell, S. W., Grasser, W. A., & Murphy, D. B. (1986). End-to-end annealing of
645 microtubules in vitro. *The Journal of Cell Biology*, *102*(2), 619□627.
646 https://doi.org/10.1083/jcb.102.2.619

647 Sawin, K. E., & Mitchison, T. J. (1994). Microtubule flux in mitosis is independent of
648 chromosomes, centrosomes, and antiparallel microtubules. *Molecular Biology of the Cell*,
649 *5*(2), 217–226. https://doi.org/10.1091/mbc.5.2.217
650 Schaedel, L., Triclin, S., Chrétien, D., Abrieu, A., Aumeier, C., Gaillard, J., Blanchoin, L.,
651 Théry, M., & John, K. (2019). Lattice defects induce microtubule self-renewal. *Nature*
652 *Physics*, *15*(8), 830–838. https://doi.org/10.1038/s41567-019-0542-4
653 Song, Y. H., & Mandelkow, E. (1993). Recombinant kinesin motor domain binds to beta-
654 tubulin and decorates microtubules with a B surface lattice. *Proceedings of the National*
655 *Academy of Sciences of the United States of America*, *90*(5), 1671–1675.
656 https://doi.org/10.1073/pnas.90.5.1671
657 Song, Y. H., & Mandelkow, E. (1995). The anatomy of flagellar microtubules: Polarity,
658 seam, junctions, and lattice. *The Journal of Cell Biology*, *128*(1–2), 81–94.
659 https://doi.org/10.1083/jcb.128.1.81
660 Sosa, H., Hoenger, A., & Milligan, R. A. (1997). Three different approaches for calculating
661 the three-dimensional structure of microtubules decorated with kinesin motor domains.
662 *Journal of Structural Biology*, *118*(2), 149–158. https://doi.org/10.1006/jsbi.1997.3851
663 Théry, M., & Blanchoin, L. (2021). Microtubule self-repair. *Current Opinion in Cell Biology*,
664 *68*, 144–154. https://doi.org/10.1016/j.ceb.2020.10.012
665 Vitre, B., Coquelle, F. M., Heichette, C., Garnier, C., Chrétien, D., & Arnal, I. (2008). EB1
666 regulates microtubule dynamics and tubulin sheet closure in vitro. *Nature Cell Biology*, *10*(4),
667 415–421. https://doi.org/10.1038/ncb1703
668 Wade, R. H., & Chrétien, D. (1993). Cryoelectron microscopy of microtubules. *Journal of*
669 *Structural Biology*, *110*(1), 1–27. https://doi.org/10.1006/jsbi.1993.1001
670 Zabeo, D., Heumann, J. M., Schwartz, C. L., Suzuki-Shinjo, A., Morgan, G., Widlund, P. O.,
671 & Höög, J. L. (2018). A lumenal interrupted helix in human sperm tail microtubules.

672 *Scientific Reports*, *8*(1), 2727. https://doi.org/10.1038/s41598-018-21165-8

673 Zhang, R., Alushin, G. M., Brown, A., & Nogales, E. (2015). Mechanistic Origin of

674 Microtubule Dynamic Instability and Its Modulation by EB Proteins. *Cell*, *162*(4), 849□859.

675 https://doi.org/10.1016/j.cell.2015.07.012

676

677

Figures

Figure 1

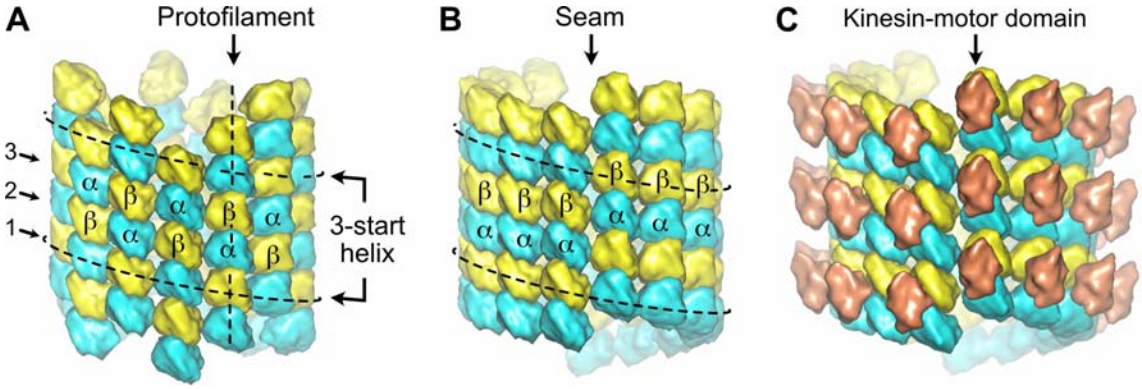

Organization of tubulin within microtubules

The αβ-tubulin heterodimers (α in cyan, β in yellow) alternate head-to-tail along protofilaments, 13 of which associate laterally to form the microtubule wall. **(A)** In the A-type lattice, the lateral contacts are made between heterotypic subunits (α-β, β-α) along the 3-start helices. **(B)** In the B-type lattice, the lateral contacts are made between homotypic subunits (α-α, β-β), except at one unique region of the A-type called the seam. **(C)** Decoration of microtubules with kinesin-motor domains (orange) that bind to β-tubulin highlights the organization of the tubulin heterodimer within microtubules.

Figure 2

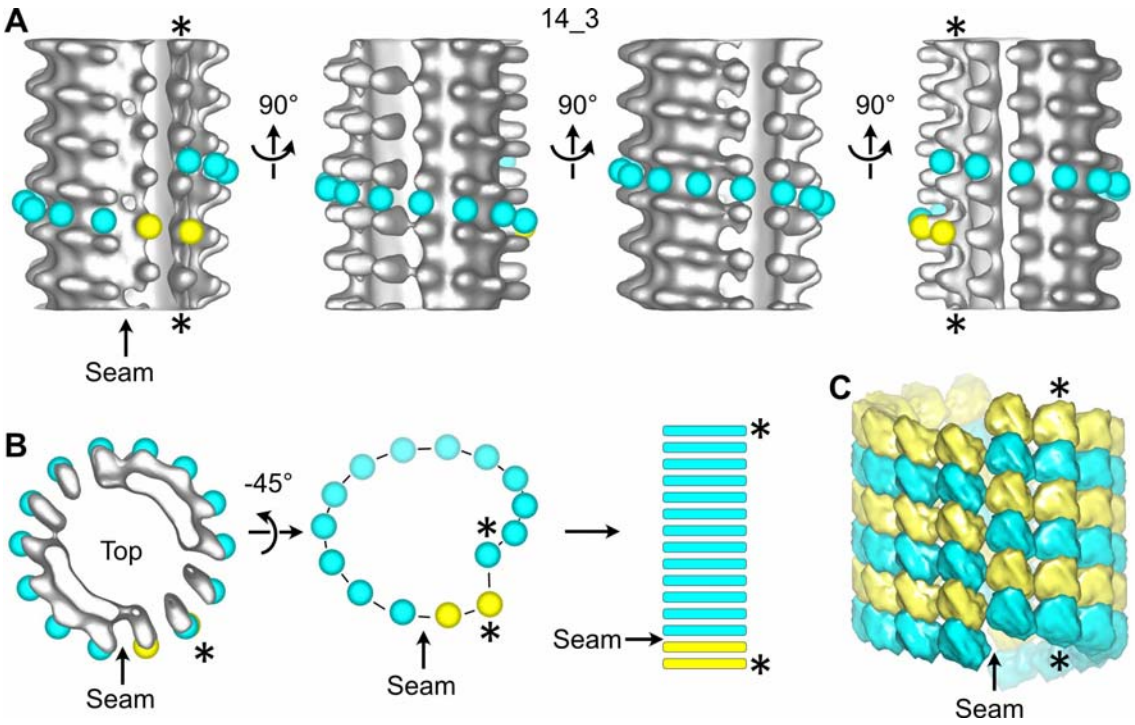

Sub-tomogram averaging of a 14_3 microtubule with a unique seam

(A) Sub-tomogram average of a 1390.4 nm long 14_3 microtubule assembled *in vitro* from purified tubulin and decorated with kinesin-motor domains (Figure 2 - figure supplement 3A: MT3, Video 2). The panel displays 4 views turned by 90° with respect to the longitudinal axis of the microtubule. Yellow spheres have been placed onto the kinesin-motor domain densities and cyan spheres in between them. They follow the left-handed, three-start helix of the microtubule lattice. The seam shows up as a change in color from yellow to cyan. **(B)** Symbolic representation of the microtubule lattice. The top view of the microtubule in (A) is turned by 45° around the X-axis and the density is masked to reveal the organization of the tubulin subunits in one turn of the three-start helix. The helix is unrolled and represented as longitudinal bars that correspond to the organization of the αβ-subunits in microtubule segments. **(C)** 3D model of the underlying tubulin dimer lattice. The stars (*) indicate the same protofilament in (A-C).

706 **Figure 3**

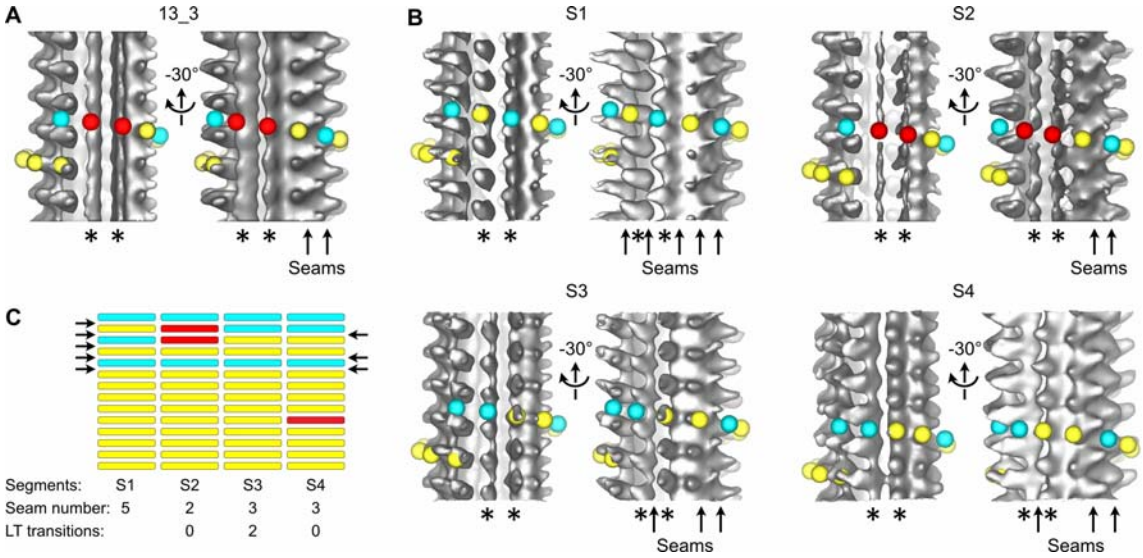

707

708 **Transition in seam number within a 13_3 microtubule**

709 **(A)** Average of a 1327.2 nm long 13_3 microtubule displaying two aberrant protofilaments
710 (*), and two adjacent seams (arrows in the -30° view). Red spheres have been placed on top
711 of the aberrant protofilaments. **(B)** Segmented sub-tomogram averaging of the microtubule in
712 (A). The microtubule has been divided into 4 segments of 331.8 nm in length, and sub-
713 tomogram averages have been calculated for each segment (S1 to S4). The two aberrant
714 protofilaments in (A) are well resolved in S1, S3 and S4, while they still display an aberrant
715 shape in S2. The lattice organization of these protofilaments must be offset by at least one
716 tubulin subunit between S1 and S3. Hence, S2 constitutes a transition zone where kinesin-
717 motor domain densities and absence of densities have been averaged. **(C)** Flat representation
718 of the lattice organization within segments S1 to S4. S1 contains 5 seams while S3 and S4
719 contain 3 seams (arrows). Two lattice type (LT) transitions occur between S1 and S3, and S4
720 contains an aberrant protofilament (Video 3). A finer segmentation of the microtubule at
721 165.9 nm revealed an additional lattice type transition in this region (Figure 3 - figure
722 supplement 3A: MT5, between segments S5 and S7).

723

724 **Figure 4**

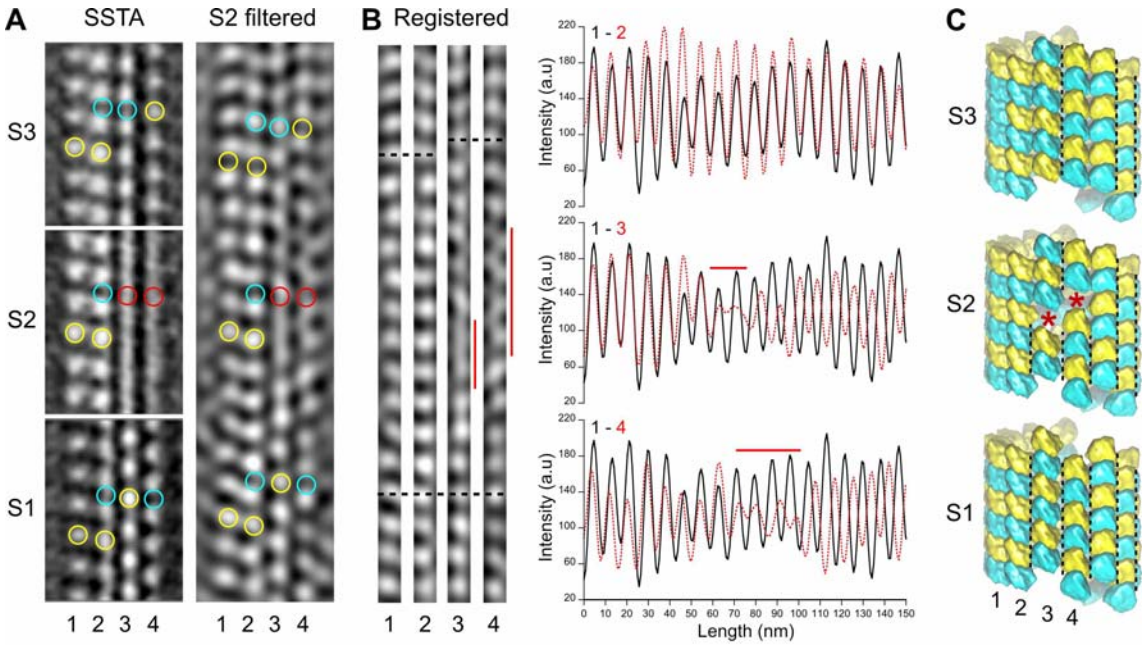

725

726 **Comparison between SSTA and Fourier filtered images of transition regions**

727 **(A)** SSTA: slices through the sub-tomogram averages of segments S1 to S3 in Figure 3B

728 (*left*). The contrast has been inverted with respect to the original tomogram to represent

729 protein densities as white. Yellow open circles have been placed on kinesin-motor domain

730 densities, cyan open circles in between them, and red open circles on aberrant densities in S2.

731 S2 filtered: slice through the filtered tomogram of the S2 region (*right*). The change in lattice

732 seam number from S1 to S3 is clearly visualized in the S2 region. **(B)** Protofilaments 1 to 4 in

733 (A) have been extracted from the filtered image and put into register (Registered, *left*). They

734 remain in phase (bottom dotted line) until the densities in protofilaments 3 and 4 becomes

735 fuzzy (vertical red lines). After theses transition zones, the kinesin-motor domain periodicity

736 in protofilaments 3 and 4 becomes out of phase with respect to that in protofilaments 1 and 2

737 (upper dotted lines). These changes in kinesin-motor domain periodicity are confirmed in the

738 line plots of the protofilaments (*right*). While the kinesin-motor domain periodicity in

739 protofilaments 1 and 2 remain perfectly in phase (*upper graph*), it becomes out of phase for

740 protofilaments 3 and 4 after the transition zones (*middle and bottom graphs*). **(C)** Schematic

741 representation of the αβ-tubulin heterodimer organization in segments S1 to S3. The
742 transition from 5 seams in S1 to 3 seams in S3 requires an offset of at least one monomer (red
743 stars) in the protofilaments 3 and 4 of S2. Black dotted lines highlight the seams in each
744 segment.
745

746 **Figure 5**

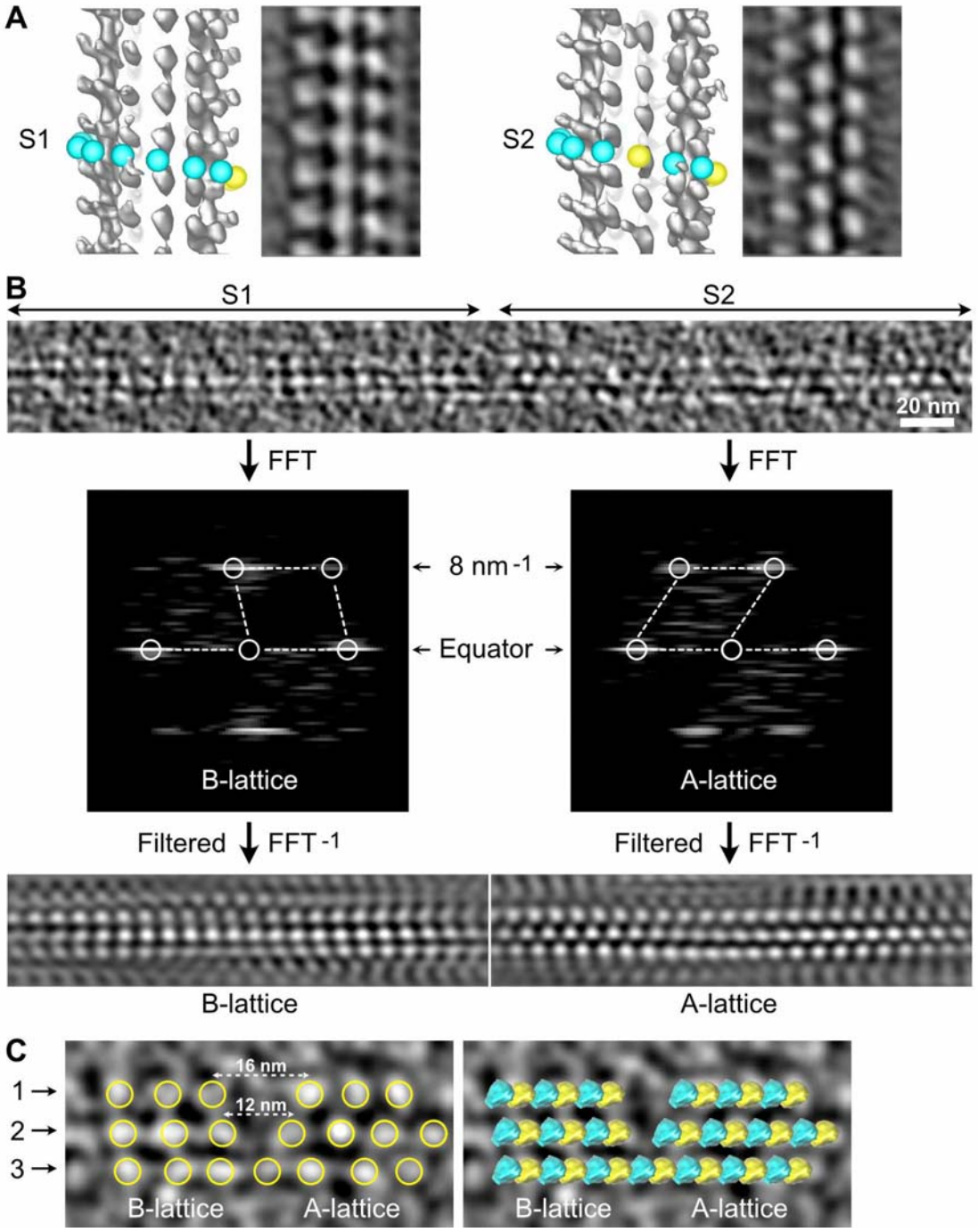

747

748 **Direct visualization of holes within microtubules**

749 **(A)** Sub-tomogram average segments before (S1) and after (S2) a lattice type transition in a

750 GMPCPP-microtubule. For each segment, the isosurface of the full volume (*left*) and a slice

751 through the sub-tomogram average (*right*) are displayed. The contrast has been inverted to

represent protein density as white. S1 and S2 contain 1 and 3 seams, respectively. **(B)** Z-projection of 20 slices at the surface of the microtubule that encompasses S1 and S2 (*top*) with their associated Fourier transforms (*middle*) and filtered versions of the corresponding regions after selection of the equatorial and 8 nm^{-1} layer lines (*bottom*). The 3 protofilaments in S1 and S2 are organized according to a B- and an A-lattice, respectively. **(C)** Enlarged central region of the microtubule in (B). Yellow open circles have been placed on the kinesin densities (*left*), showing a gap of one subunit in protofilament 2, and possibly of a dimer in protofilament 1, although an absence of kinesin-motor domain at this location cannot be excluded. Tubulin heterodimers have been placed at the corresponding location (*right*) to highlight their change in organization at the transition region.

762 **Figure 6**

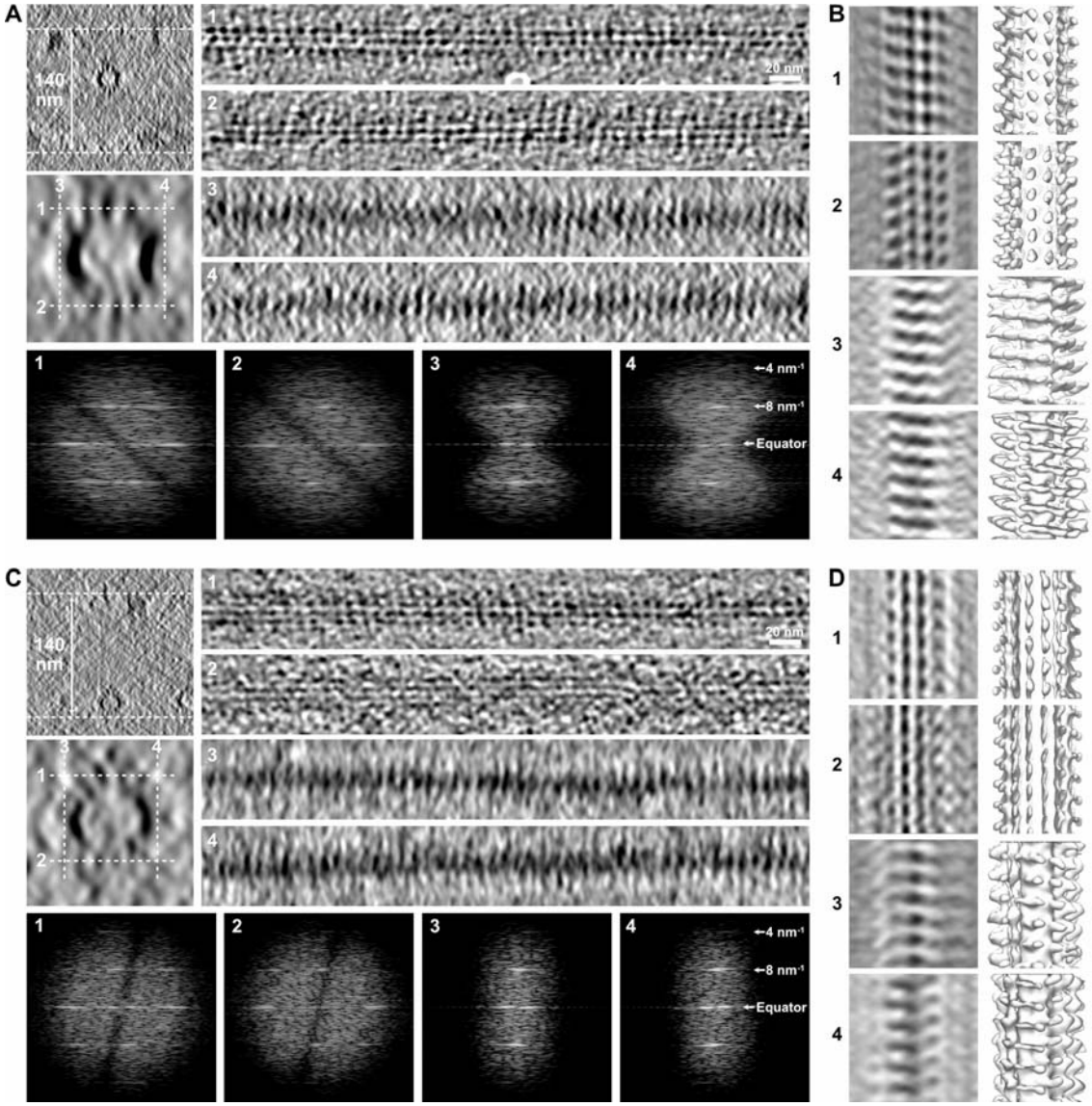

763

764 **Limitations in the visualization of holes in raw tomograms**

765 **(A)** Microtubule embedded in a ~140 nm thick ice layer (*top left*). Longitudinal sections

766 (averages of 20 slices, *right*) were performed at the top (1), bottom (2), left (3) and right (4) of

767 the microtubule at positions indicated by white dotted lines in the enlarged view of the

768 microtubule (*middle left*, average of 50 slices). Kinesin-motor domain densities can be

769 individualized on the top (1) and bottom (2) sections, but not on the edges of the microtubules

770 (3, 4) due to the elongation of densities in Z as a consequence of missing data at high angle.

771 The Fourier transforms of the corresponding segments (*bottom*) shows that the 8 nm^{-1}
772 periodicity of the kinesin-motor domains remains present in all views. **(B)** Sub-tomogram
773 average of the microtubule in (A) over 18 kinesin-motor domain repeats. Sections (*left*) and
774 isosurfaces (*right*) of the microtubule are displayed in correspondence to the longitudinal
775 sections in (A). The kinesin-motor domain position is clearly observed on the top (1) and
776 bottom (2) surfaces, and can be recovered on the microtubule edges after SSTA (3, 4). **(C)**
777 Microtubule in the same tomogram as in (A) interacting with the air-water interface (*top left*).
778 Kinesin-motor domain densities can be well discerned on the longitudinal sections (*right*) of
779 the top surface facing the solution (1), but are almost indiscernible on the bottom surface that
780 interacts with the air-water interface (2) and on the edges (3, 4). Fourier transforms (*bottom*)
781 of the corresponding segments show that the periodicity of the kinesin-motor domains is still
782 present, even on the damaged surface (2). **(D)** Sub-tomogram average of the microtubule in
783 (C) over 18 kinesin-motor domain repeats. SSTA allows recovery of the kinesin-motor
784 domain densities in all surfaces, including the one that interacts with the air-water interface
785 (2).
786

787 **Figure 7**

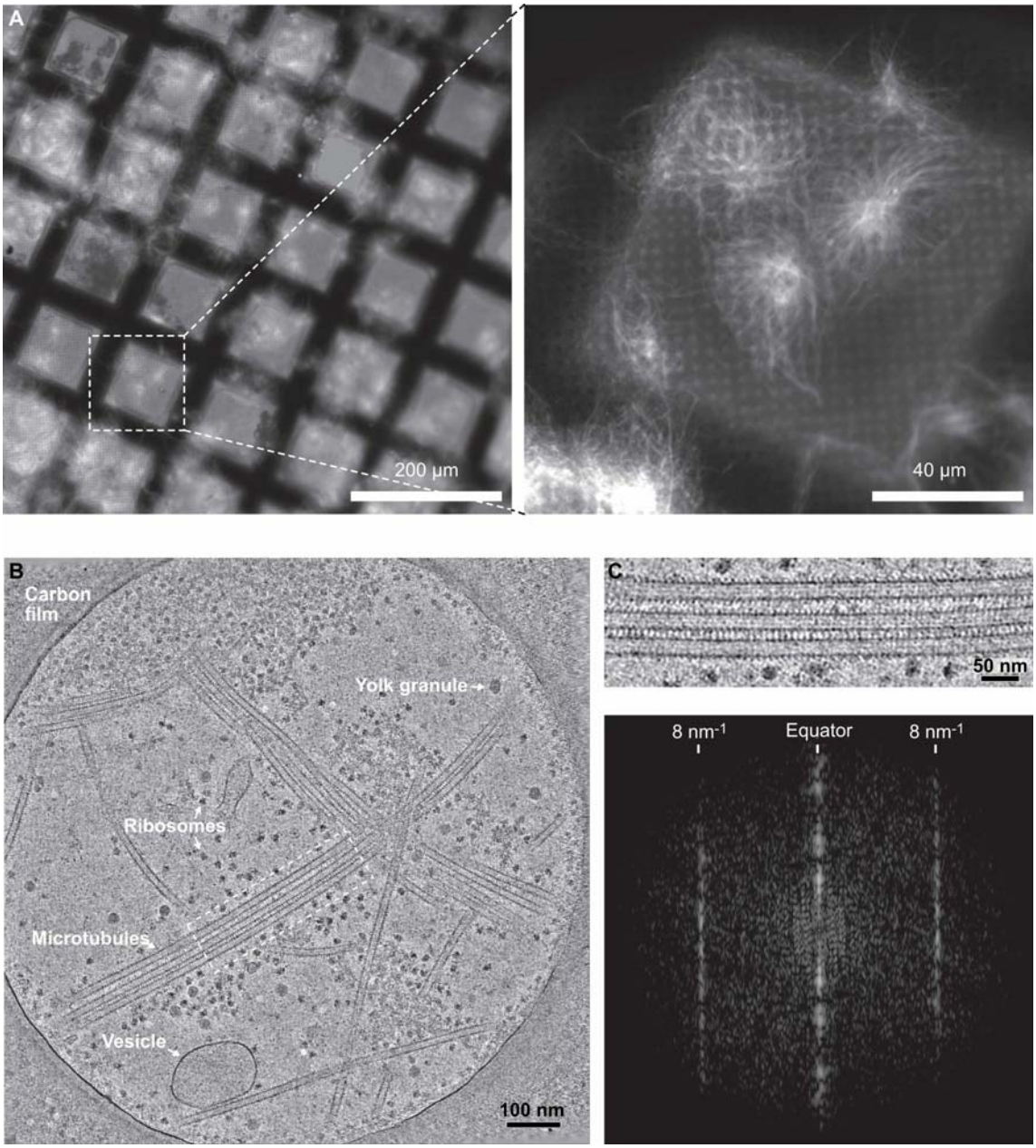

788

789 **Cryo-electron tomography of microtubules decorated by kinesin-motor domains in**

790 ***Xenopus* egg cytoplasmic extracts**

791 **(A)** Cryo-fluorescence images of microtubules assembled in a cytoplasmic extract prepared

792 from *Xenopus* eggs. Microtubules assembled in the presence of rhodamine-tubulin and

793 plunge-frozen on an EM grid were imaged using fluorescence microscopy at liquid nitrogen

794 temperature. Left: 10 X objective, right: 50 X objective. The white dashed square on the 10 X

795 image indicates the field of view of the 50 X image. **(B)** Average of 30 slices in Z through a
796 cryo-electron tomogram. The thin layer of cytoplasm spans a 2 µm diameter hole of the
797 carbon film. The main visible features are ribosomes, vesicles, yolk granules and
798 microtubules decorated by kinesin-motor domains. **(C)** *Top*, enlargement of the dotted
799 rectangular region in (B) (Video 4). *Bottom,* Fourier transform of the top image showing
800 strong layer lines at 8 nm^{-1} corresponding to the kinesin-motor domain repeat along the
801 microtubules.
802

Figure 8

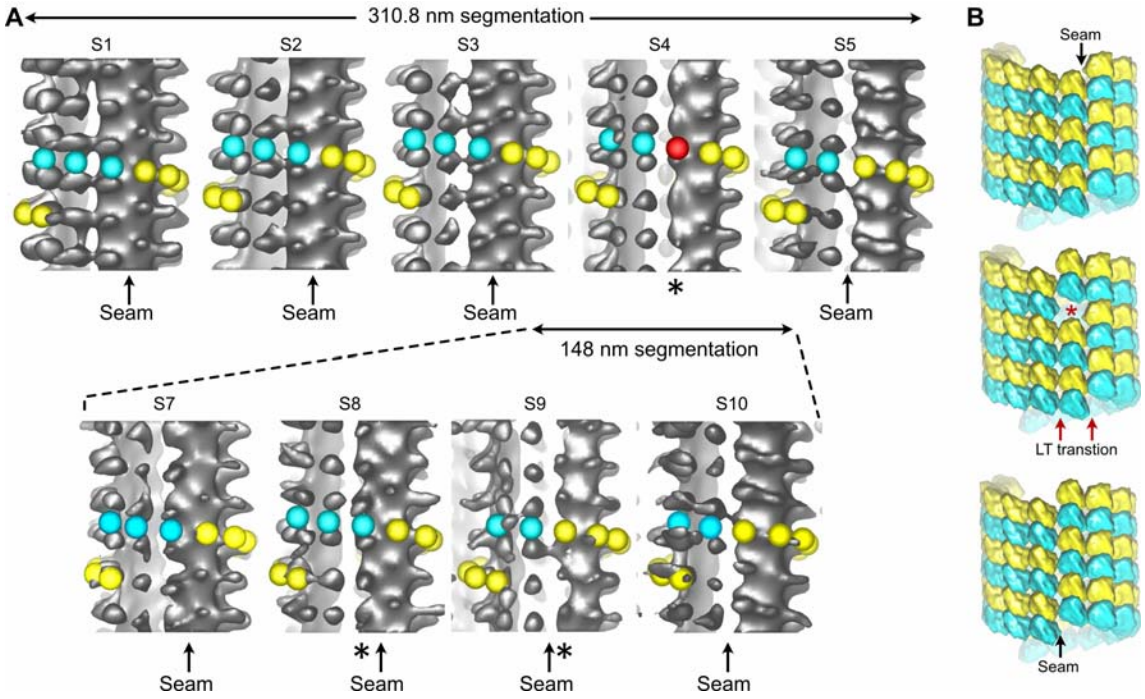

SSTA of microtubules decorated by kinesin-motor domains in *Xenopus* egg cytoplasmic extracts

(A) Sub-tomogram averages of five 310.8 nm long segments of a 13_3 microtubule (original length 1628 nm, *top*). S4 contains an aberrant protofilament (*), and the seam (arrow) moves laterally to the left by one protofilament from S3 to S5. The microtubule has been segmented into eleven 148 long segments (*bottom*, Figure 8 - figure supplement 5A: MT2). Only S7 to S10 are shown, corresponding to a region that encompass S3 to S5 in the 310.8 nm segmentation (Video 5). The lattice type transition occurs from S8 to S9, and no aberrant protofilament is observed in this finer segmentation. **(B)** 3D models of the tubulin lattice before (*top*), during (*middle*) and after (*bottom*) the transition. The lateral offset in seam position requires a longitudinal offset of a minimum of one tubulin subunit to account for the lattice type transition observed in (A).

818 **Figure 9**

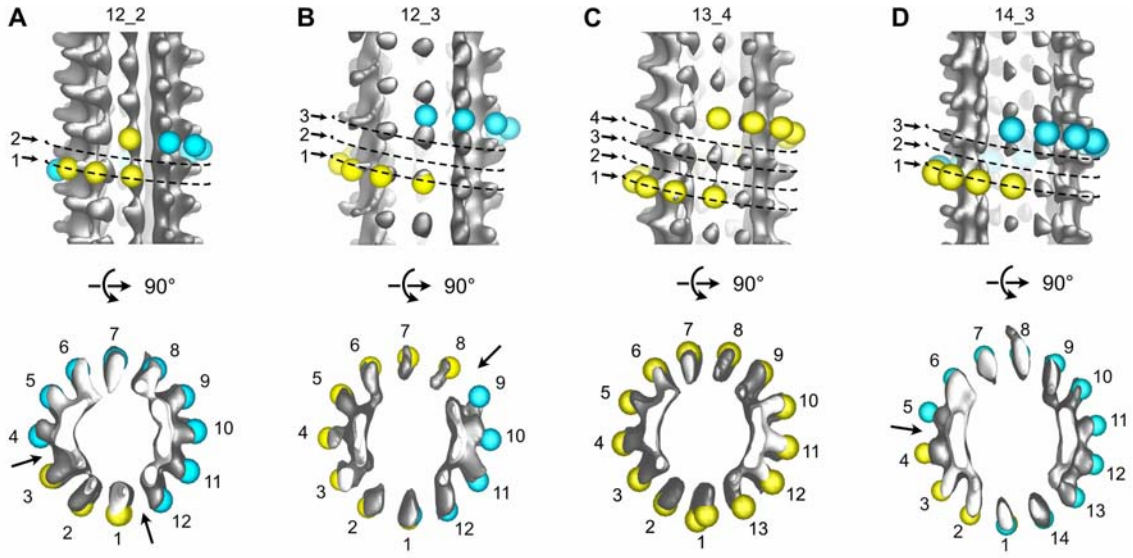

819

820 **Variations in protofilament and helix-start numbers in microtubules assembled in**

821 ***Xenopus* egg cytoplasmic extracts**

822 **(A)** 12_2 microtubule with two seams (Figure 9 - figure supplement 5A: MT9). **(B)** 12_3

823 microtubule with a unique seam. This microtubule transitioned to a 13_3 configuration

824 (Figure 9 - figure supplement 5D: MT62). **(C)** 13_4 microtubule with no seam. This

825 microtubule transitioned to a 13_3 configuration (Figure 9 - figure supplement 5A: MT7). **(D)**

826 14_3 microtubule with one seam. This microtubule transitioned to a 13_3 configuration

827 (Figure 9 - figure supplement 5B: MT32).

828

829 **Figure 10**

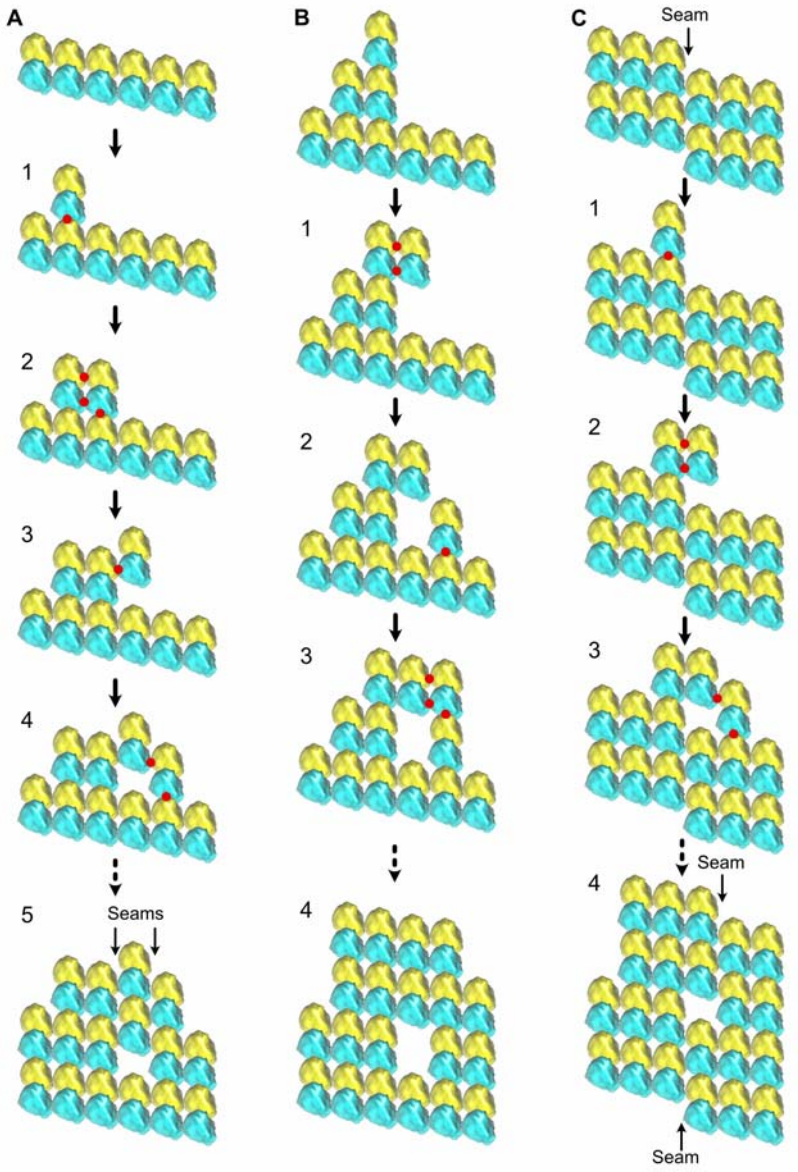

830

831 **Formation of holes within microtubules during assembly**

832 **(A)** Formation of multiple seams, red dots indicate new interactions. 1) Unique longitudinal

833 interaction. 2) Combined lateral and longitudinal interactions. 3) Unique lateral interaction

834 between one α-tubulin subunit of an incoming tubulin dimer and a β-tubulin subunit at the tip

835 of the growing microtubule. 4-5) Incorporation of a hole within the microtubule lattice. Two

836 A-lattice seams have been formed (arrows). **(B)** Incorporation of a tubulin dimer gap without

837 change in lattice type organization. 1) Homotypic lateral interaction of an incoming tubulin
838 dimer without longitudinal interaction. 2-5) Incorporation of a tubulin dimer gap inside the
839 microtubule lattice. **(C)** Lateral offset of the seam by one protofilament during elongation. 1)
840 Unique longitudinal interaction. 2) Homotypic interaction of an incoming dimer at the seam
841 region without longitudinal contact. 3-4) Incorporation of a lattice type transition inside the
842 microtubule wall. The seam has moved laterally by one protofilament (4), a situation
843 systematically encountered in cytoplasmic extract microtubules.
844

845 **Figure supplement 1**

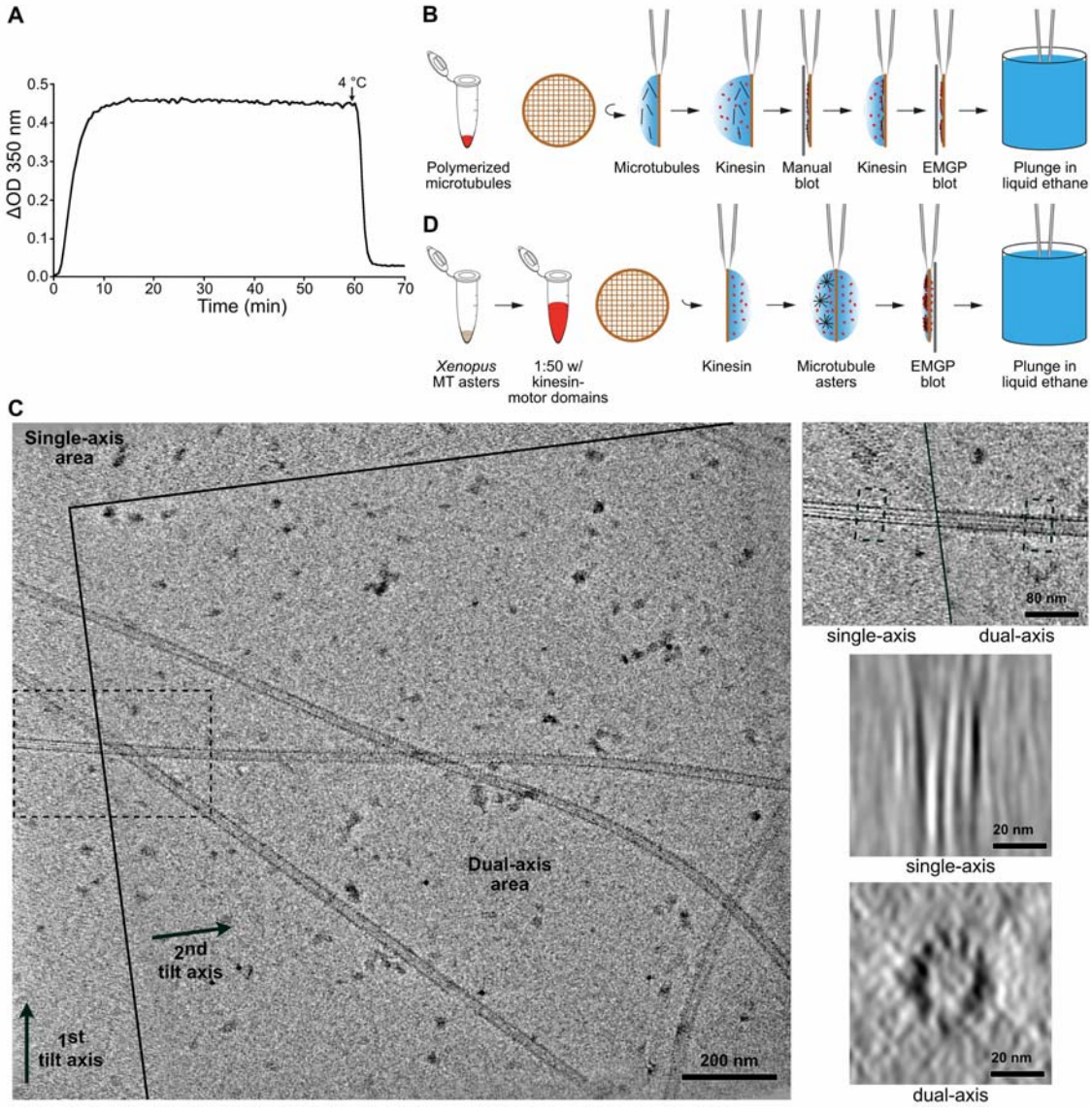

846

847 **Preparation of microtubules for cryo-electron tomography**

848 **(A)** Microtubule assembly at 40 µM tubulin in BRB80, 1 mM GTP, 35 °C. Variation of

849 optical density (ΔOD) at 350 nm versus time (min). A cooling step was typically performed at

850 the end of the experiment to assess the presence of aggregates evidenced by the value of the

851 baseline at 4 °C. Samples for cryo-electron microscopy were prepared after ~1 hour of

852 polymerization. **(B)** Decoration of microtubules assembled *in vitro* from purified tubulin with

853 kinesin-motor domains. Kinesin decoration is performed right before vitrification of the
854 sample into liquid ethane. **(C)** Dual-axis cryo-electron tomography. *Left*: The dual-axis area is
855 delimited by plain lines; arrows indicate the two tilt axes. *Right top*: Enlargement of the
856 dotted region in the overall view that encompass the single and dual axes regions of the
857 tomogram. A microtubule oriented close to the perpendicular of the 1st tilt axis spans the two
858 regions (Video 1). *Right middle*: Average of 50 slices along the microtubule in the single-axis
859 area. The microtubule is severely elongated in the Z direction. *Right bottom*: The same
860 microtubule visualized in the dual-axis area. Individual protofilaments are clearly
861 individualized. **(D)** Decoration of microtubules assembled in *Xenopus* egg cytoplasmic
862 extracts. Microtubule asters are deposited on one side of the grid, which is subsequently
863 blotted from the opposite side.
864

865 **Figure supplement 2**

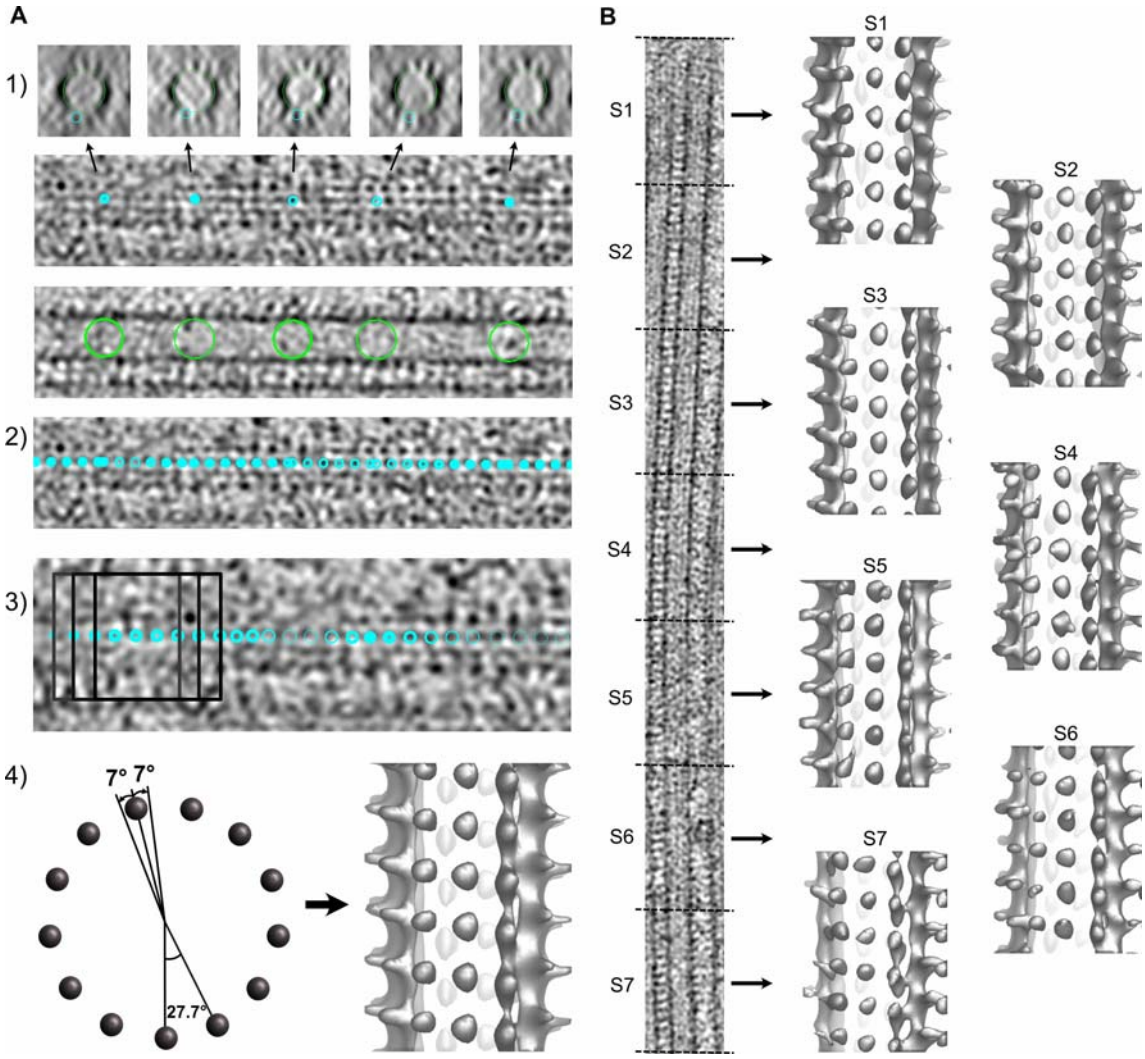

866

867 **Segmented sub-tomogram averaging of microtubules decorated with kinesin motor**

868 **domains**

869 **(A)** Sub-tomogram averaging (STA). (1) A first model is created by placing model points

870 onto individual protofilaments (small cyan circles) and at the microtubule center (large green

871 circles). (2) A second model is extrapolated from the previous one with points spaced every

872 ~8 nm along the microtubule. (3) Sub-volumes (dark squares) are extracted at every point

873 position and aligned by cross-correlation using PEET. (4) The rotational search around the

874 microtubule axis is restricted to about half the angular separation between protofilaments

875 (*left*). The resulting average is displayed in isosurface rendering in IMOD (*right*). **(B)**

876 Segmented sub-tomogram averaging (SSTA). The model and motive list used to calculate the
877 whole tomogram of the microtubule is split into shorter segments of equal dimensions and
878 sub-tomograms are calculated for each segment (S1 to S7). The segment size is limited by the
879 signal-to-noise ratio present in the tomograms (typically ~160 nm with our current data).
880

881 **Figure supplement 3A**

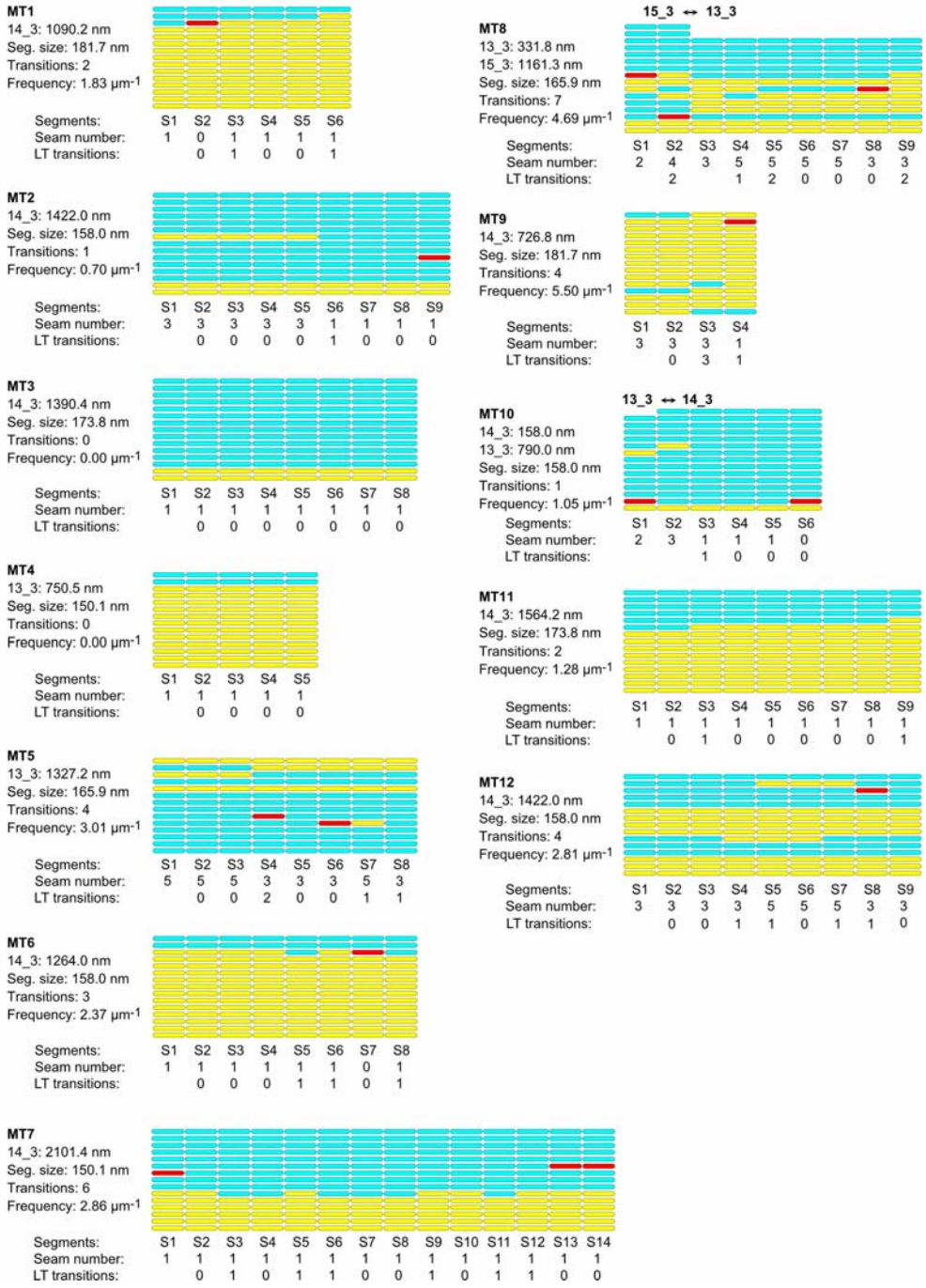

882

883 **Figure supplement 3B**

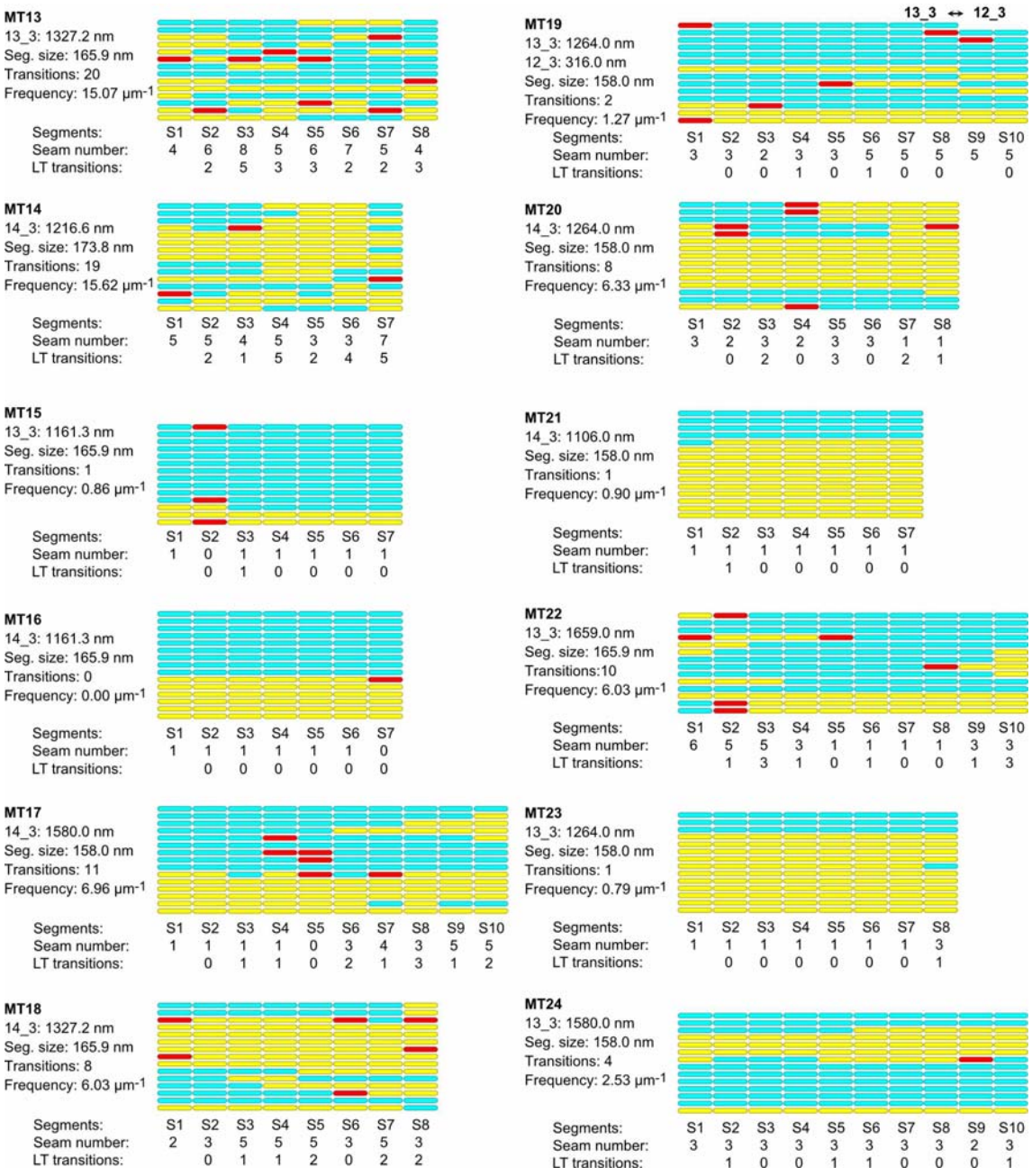

884

885 **Lattice organization of microtubules assembled *in vitro* from purified porcine brain**

886 **tubulin in the presence of GTP**

887 24 microtubules (31.7 µm in total length) were analyzed on 4 tomograms acquired on 2

888 independent samples. Number of microtubule segments: 195; number of lateral interactions:

889 2664 (A type: 461, B type: 2091, ND: 112); lattice type transitions: 119;

890 protofilament/helical-start (*N/S*) number transitions: 3.

891

892 **Figure supplement 4A**

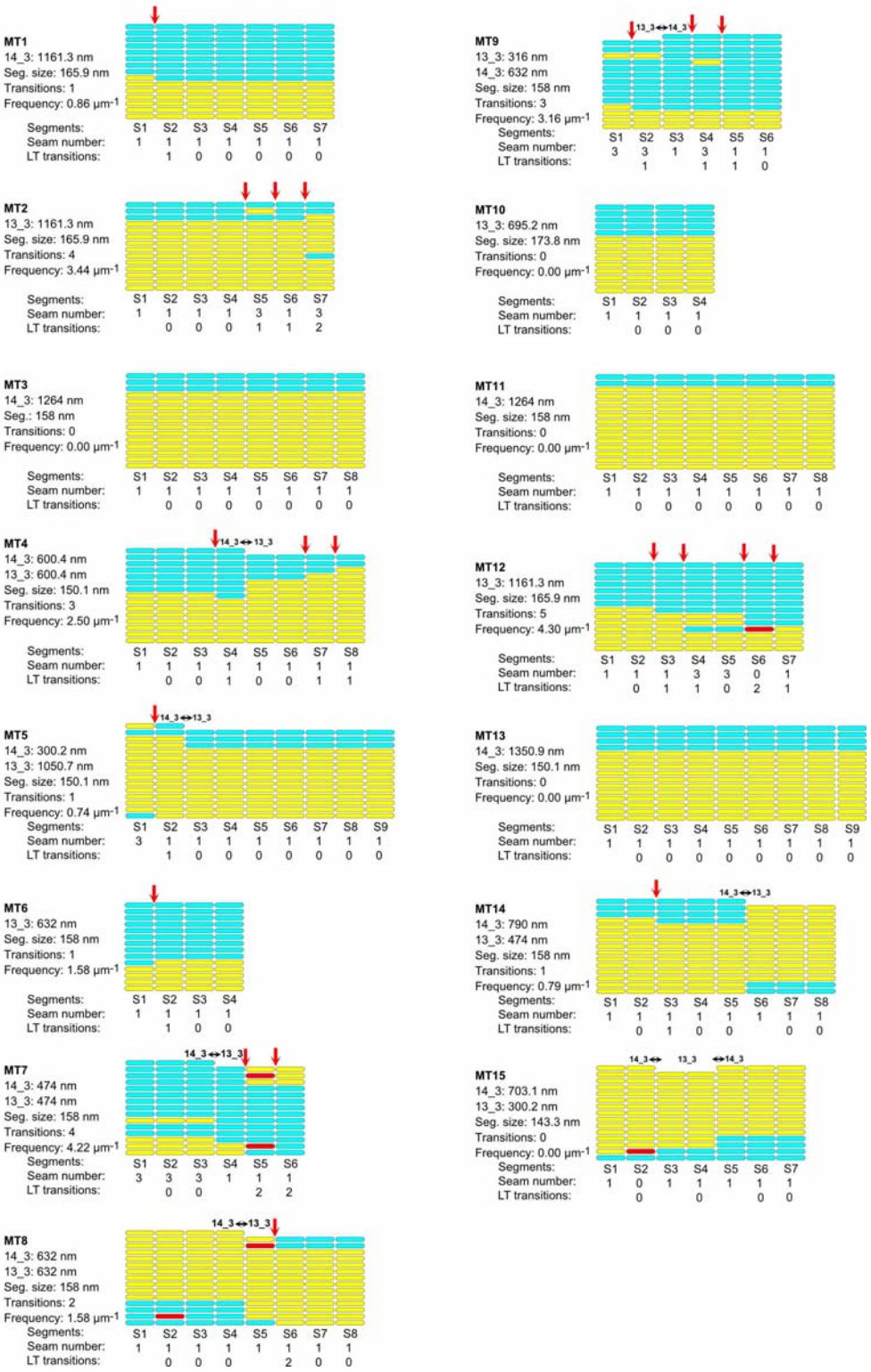

893

894

Figure supplement 4B

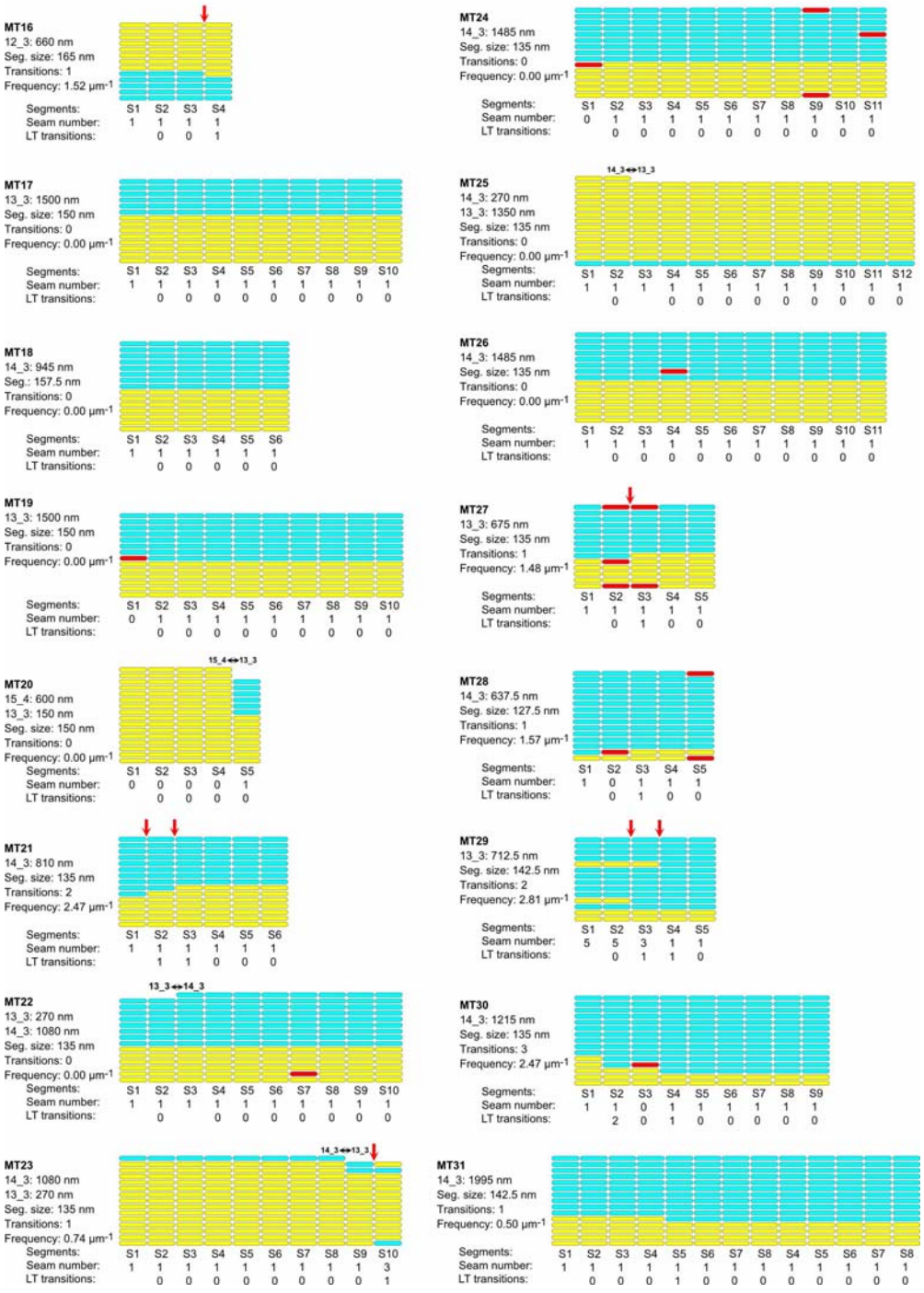

Lattice organization of microtubules assembled *in vitro* from purified porcine brain tubulin in the presence of GMPCPP

899 31 microtubules (35.4 µm in total length) were analyzed on 6 tomograms acquired on 2

900 independent samples. Number of microtubule segments: 239; number of lateral interactions:

901 3250 (A type: 261, B type: 2951, ND: 38); lattice type (LT) transitions: 37;

902 protofilament/helical-start (*N/S*) number transitions: 12.

903

Figure supplement 5A

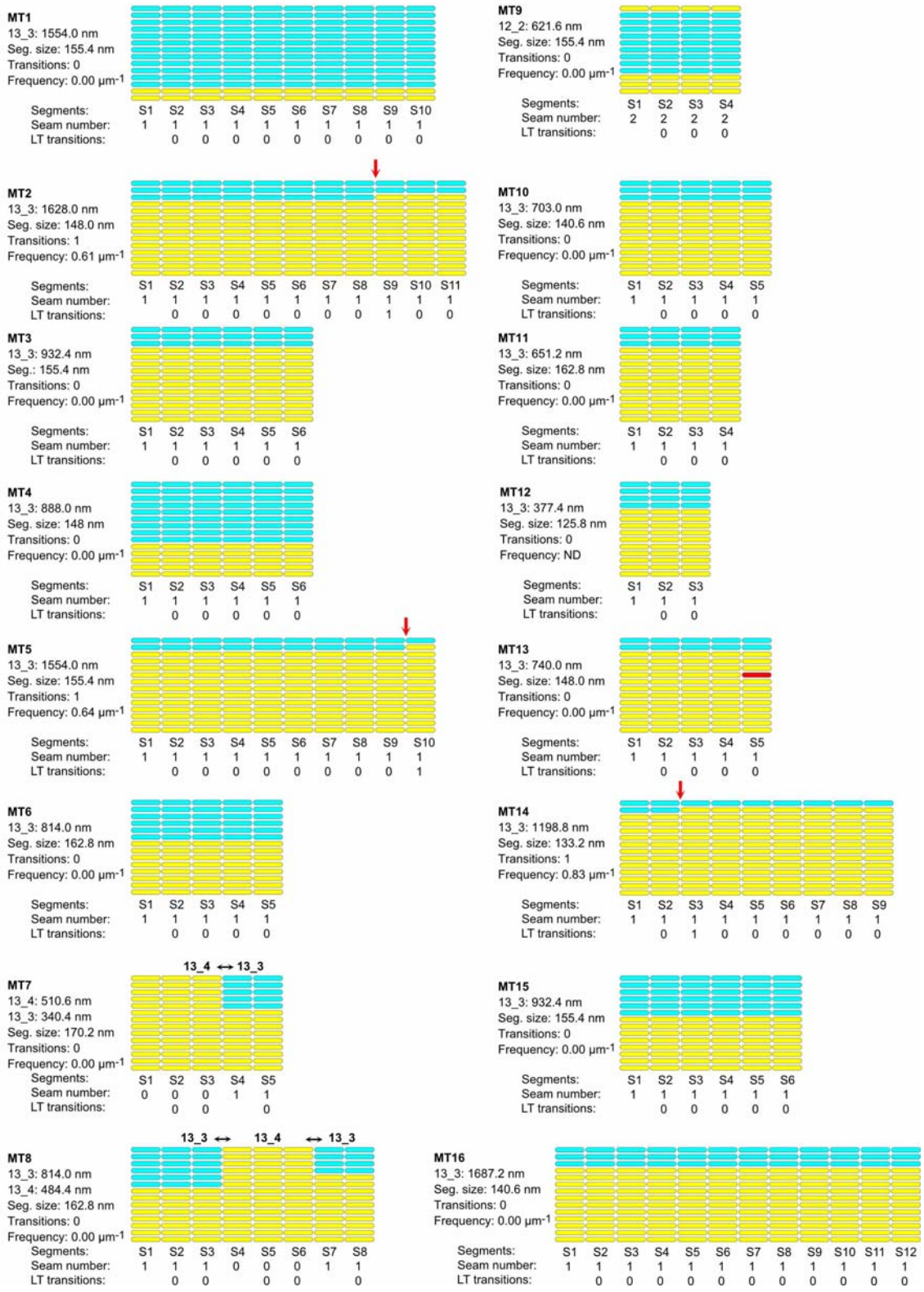

907 **Figure supplement 5B**

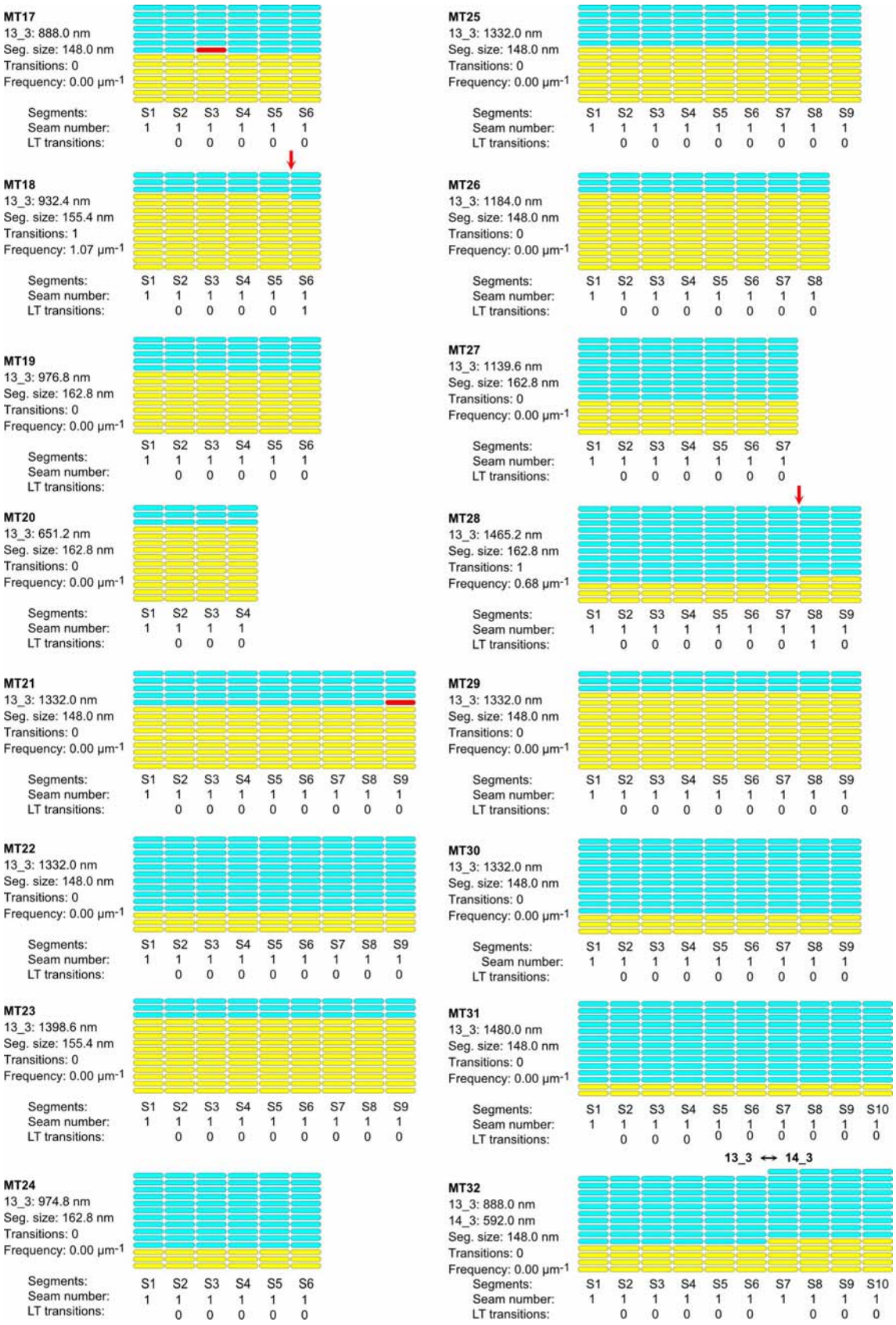

908

Figure supplement 5C

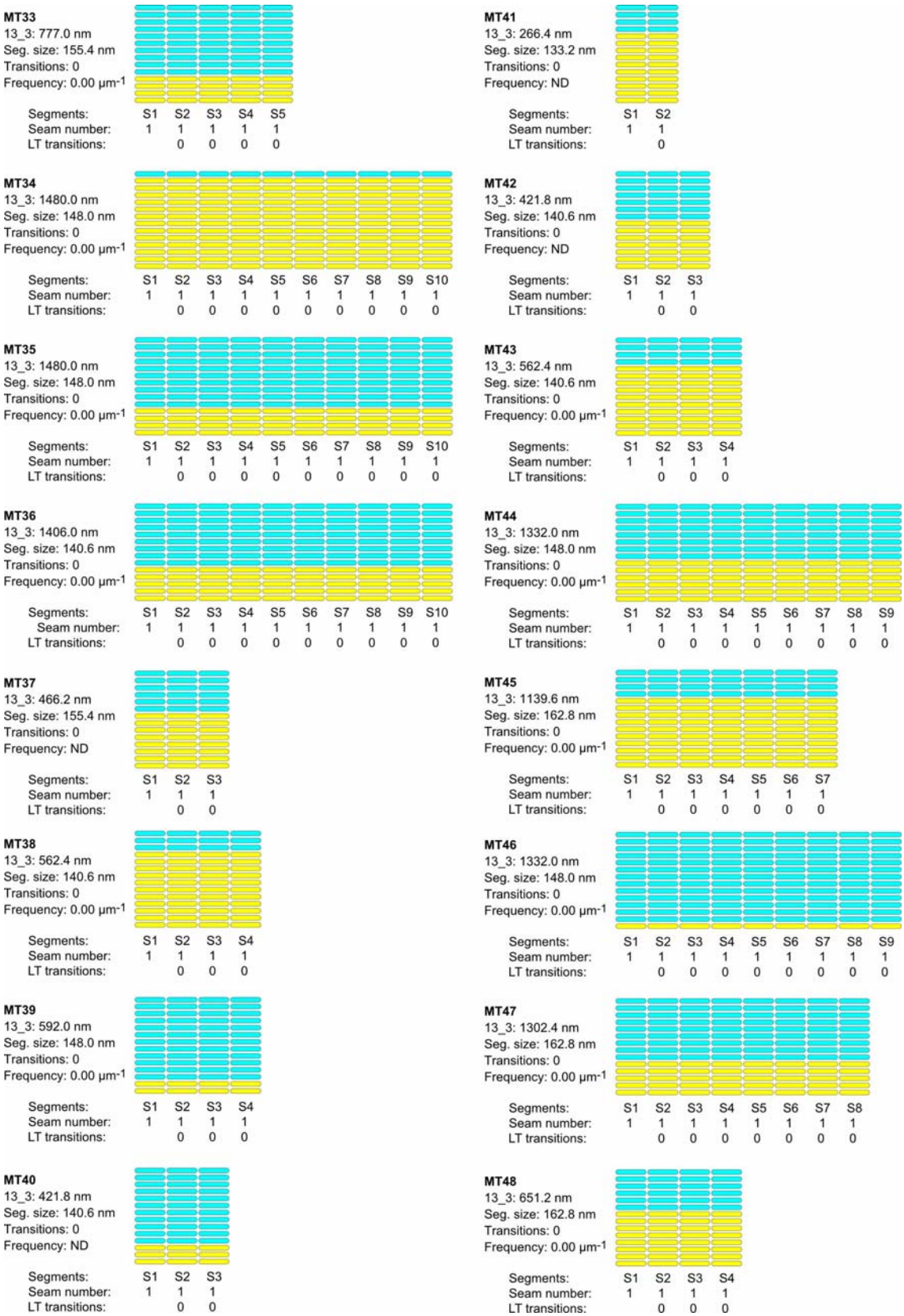

911 **Figure supplement 5D**

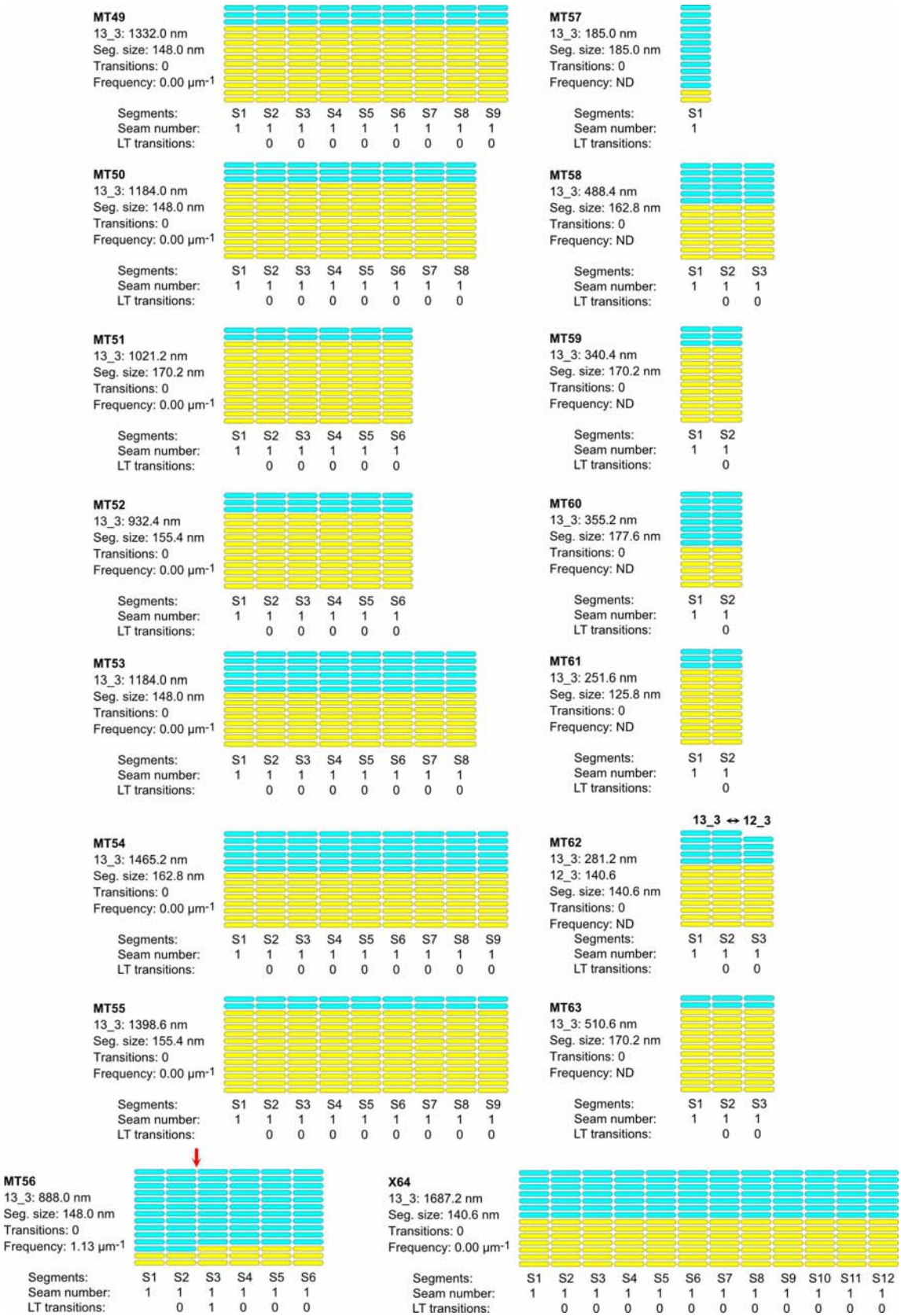

912

Lattice organization of microtubules assembled in cytoplasmic *Xenopus* egg extracts in the presence of 5% DMSO

64 microtubules (63.5 µm in total length) were analyzed on 5 tomograms acquired on one sample. Number of microtubule segments: 419; number of lateral interactions: 5446 (A type: 414, B type: 5024, ND: 8); lattice type (LT) transitions: 6; protofilament/helical-start (*N/S*) number transitions: 5. Red arrows indicate lattice type transitions in MT2, MT5, MT14, MT18, MT28 and MT56.

Figure supplement 6

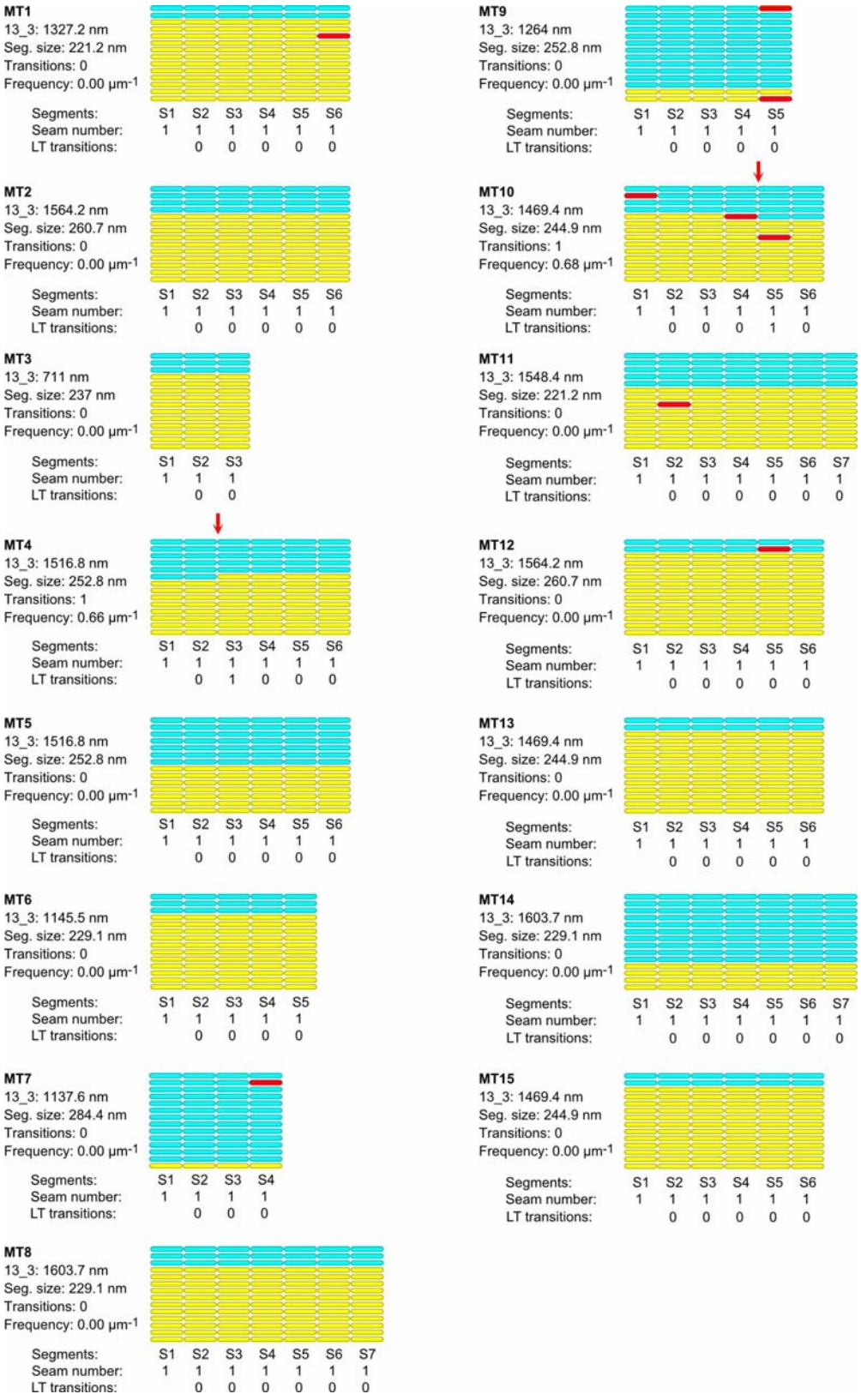

Lattice organization of microtubules assembled in cytoplasmic *Xenopus* egg extracts in the presence of RanQ69L

15 microtubules (20.6 µm in total length) were analyzed on 1 tomogram acquired on one sample. Number of microtubule segments: 86; number of lateral interactions: 1118 (A type: 8, B type: 1018, ND: 16); lattice type (LT) transitions: 2. Red arrows indicate lattice type transitions in MT4 and MT10.

930 **Supplementary Table 1. Characterization of microtubule lattice structure by cryo-**
931 **electron tomography and segmented sub-tomogram averaging**
932

Assembly conditions	GTP	GMPCPP	*Xenopus* DMSO	*Xenopus* RanQ69L
Tomograms	4	6	5	1
Samples	2	2	1	1
Microtubules	24	31	64	15
Total length (µm)	31.7	35.4	63.5	20.6
Segments	195	239	419	86
Lateral interactions	2664	3250	5446	1118
A-type	461	261	414	8
B-type	2091	2951	5024	1018
ND	112	38	8	6
Lattice-type transitions	119	37	6	2
Frequency (μm^{-1})	3.69 ± 4.20	1.24 ± 1.41	0.10 ± 0.28	0.13 ± 0.09

933
934
935 **Supplementary Table 2. Protofilament (N) and helix-start number (S)**

N_S	12_3	13_3	13_4	14_3	15_3	15_4
GTP (%)	0.99	33.07	-	64.89	1.05	-
GMPCPP (%)	1.87	39.38	-	57.06	-	1.70
Xen. DMSO (%)	1.16	96.30	1.59	0.95	-	-
Xen. RanQ69L (%)	-	100	-	-	-	-

936 *Xen.: Xenopus*

Supplementary videos

Figure 2 - Video 1. **Dual-axis cryo-electron tomography of microtubules**. Microtubule visualized in cross-section in the single- and dual-axis regions of a cryo-electron tomogram. Related to Figure 2 - figure supplement 1C.

Figure 2 - Video 2. **Sub-tomogram average of a 14_3 mono-seam microtubule**. Yellow spheres are placed on kinesin-motor domain densities and cyan spheres in between along one turn of the 3-start helix.

Figure 3 - Video 3. **SSTA of a 13_3 multi-seam microtubule**. Sub-tomogram average of the 13_3 microtubule in Figure 3A (full volume), followed by SSTA of the microtubule in 4 segments of 331.8 nm in length (Figure 3B). Red spheres are placed onto aberrant protofilaments.

Figure 7 - Video 4. **Cytoplasmic extract microtubules decorated with kinesin-motor domains.** Slices through a cryo-electron tomogram of *Xenopus* egg cytoplasm showing microtubules decorated with kinesin-motor domains.

Figure 8 - Video 5. SSTA of a 13_3 microtubule assembled in a cytoplasmic extract. SSTA of the 13_3 microtubule in Figure 8A in 310.8 nm long segments (S3-S5, Figure 8A, *top*), and 148.0 nm long segments (S7-S10, Figure 8A, *bottom*).

Figure 9 - Video 6. Sub-tomogram averages of microtubules with different protofilament and/or helix-start numbers. Sub-tomogram averages of the 12_2, 12_3,

961 13_4, 14_3 microtubules in Figure 9. Arrows point to local dislocations in the 12_2 and 13_4
962 microtubules.
963
964 **Figure 10 - Video 7. Microtubule growth-induced mechanism of lattice heterogeneity**.
965 This video depicts how holes of an odd or even number of subunits arise during microtubule
966 polymerization, with the formation of lateral interactions without longitudinal ones at the tip
967 of the growing microtubule.
968

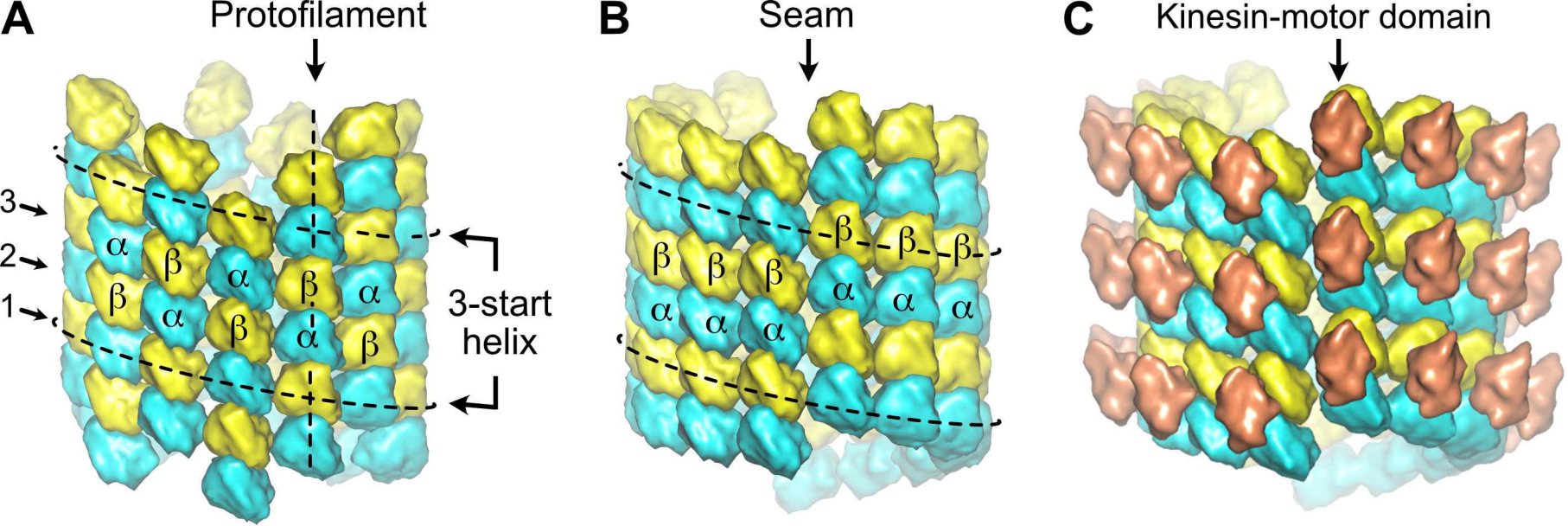
A
Protofilament
3
2
1
α
β
3-start
helix
B
Seam
C
Kinesin-motor domain

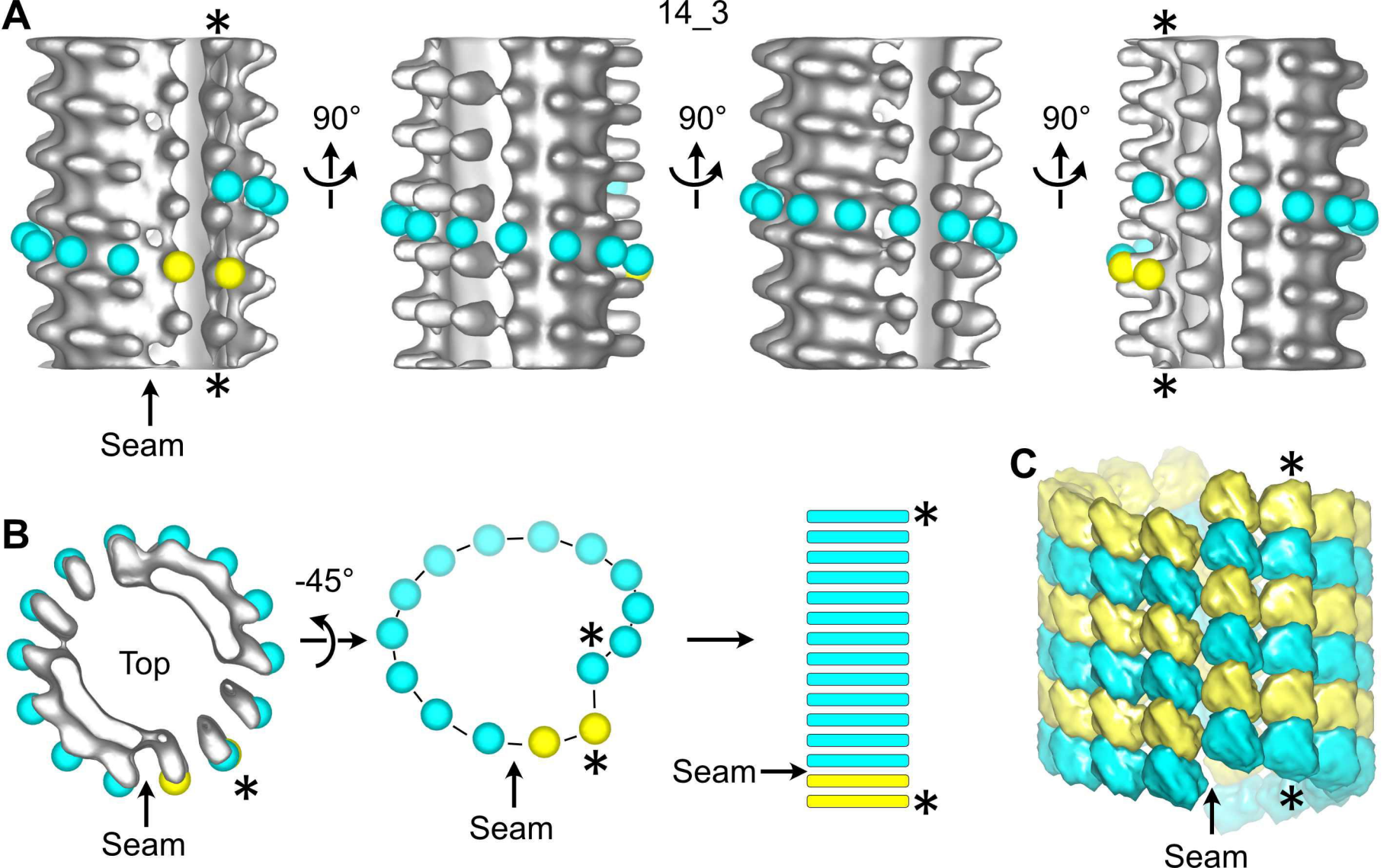
A
14_3
90°
90°
90°
Seam
B
Top
-45°
Seam
Seam
C
Seam

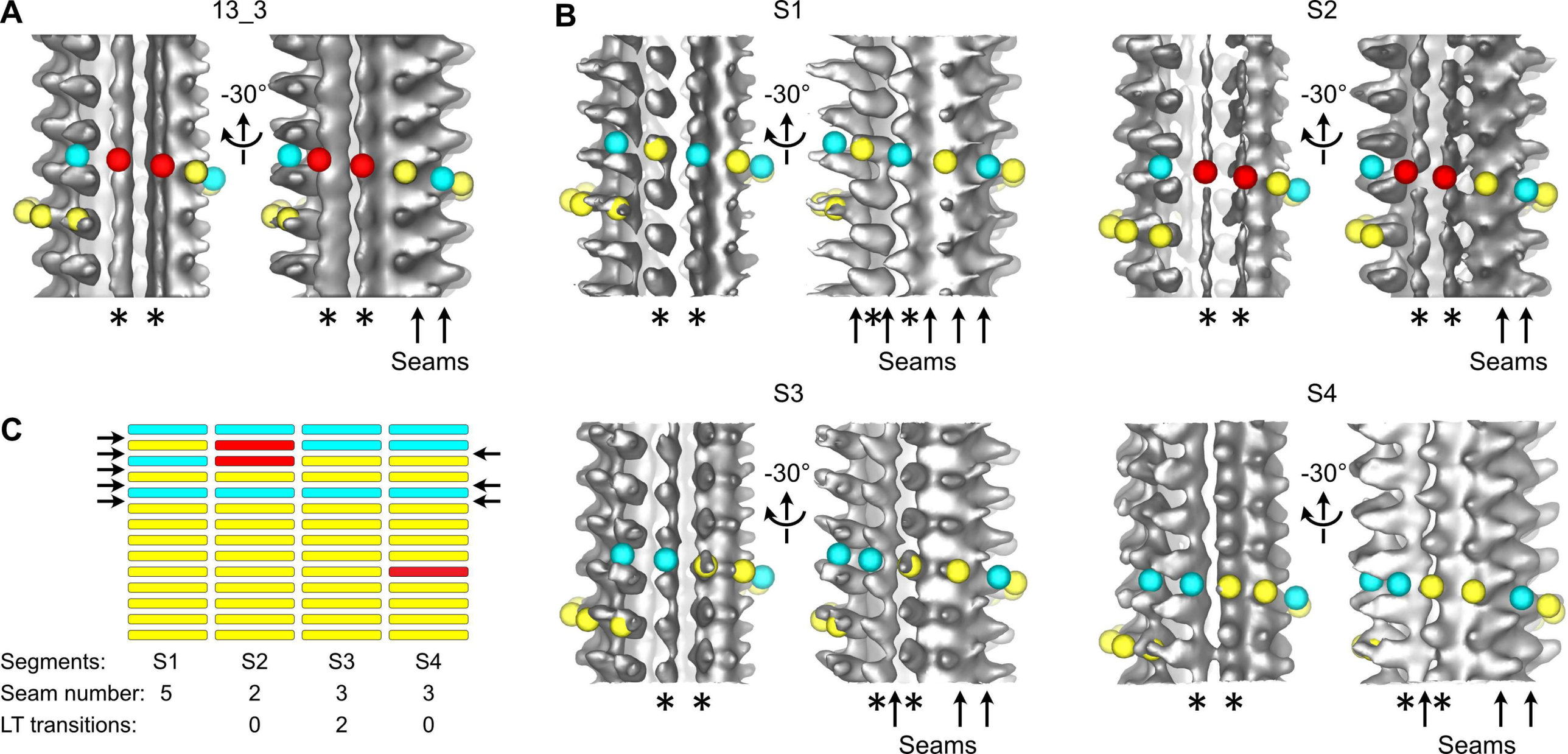
A
13_3
-30°
Seams
B
S1
-30°
Seams
S2
-30°
Seams
S3
-30°
Seams
S4
-30°
Seams
C
Segments: S1 S2 S3 S4
Seam number: 5 2 3 3
LT transitions: 0 2 0

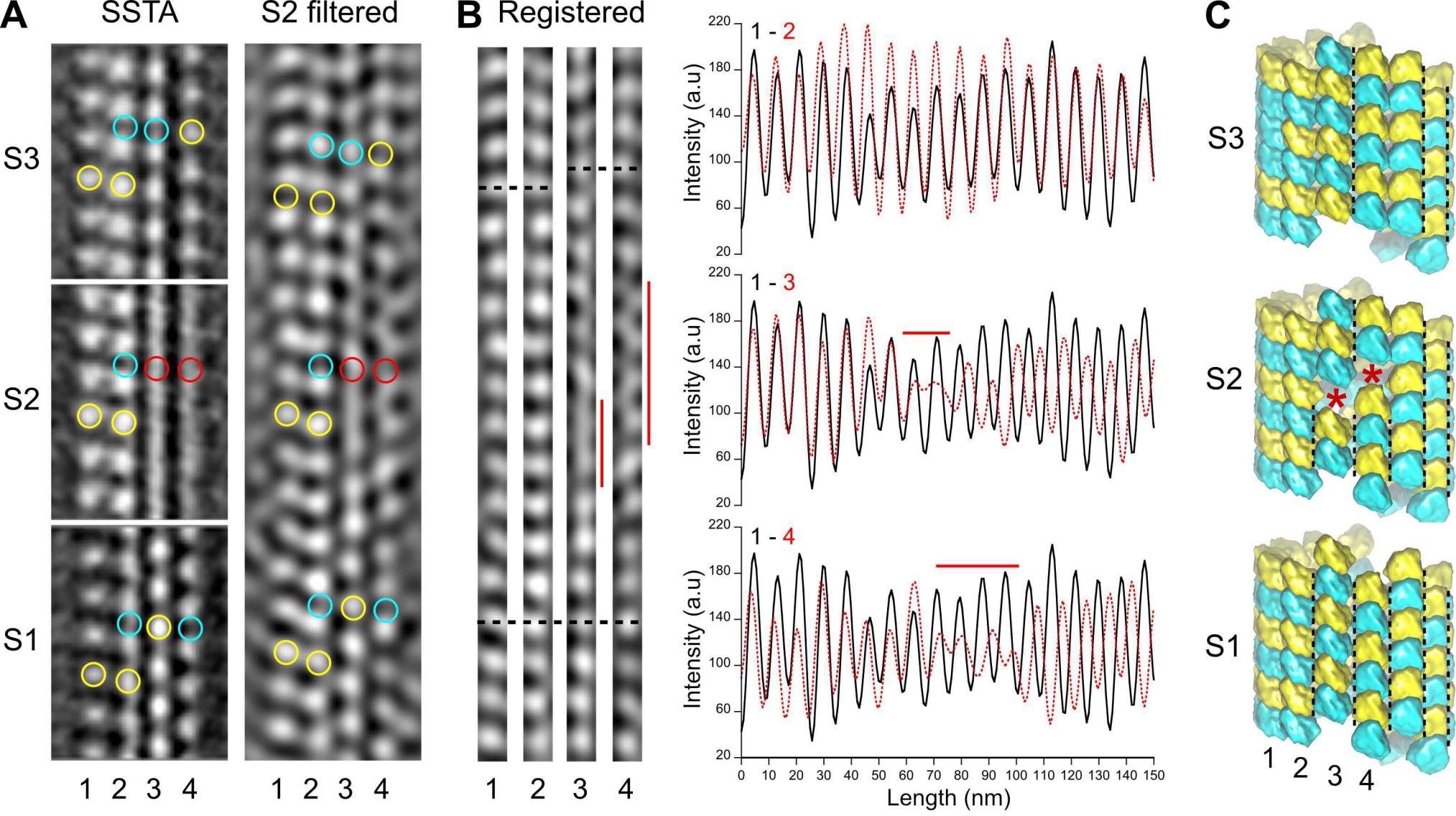
A
SSTA
S2 filtered
S3
S2
S1
1 2 3 4
1 2 3 4
B Registered
1 2 3 4
1 - 2
1 - 3
1 - 4
Intensity (a.u)
220
180
140
100
60
20
0 10 20 30 40 50 60 70 80 90 100 110 120 130 140 150
Length (nm)
C
S3
S2
S1
1 2 3 4

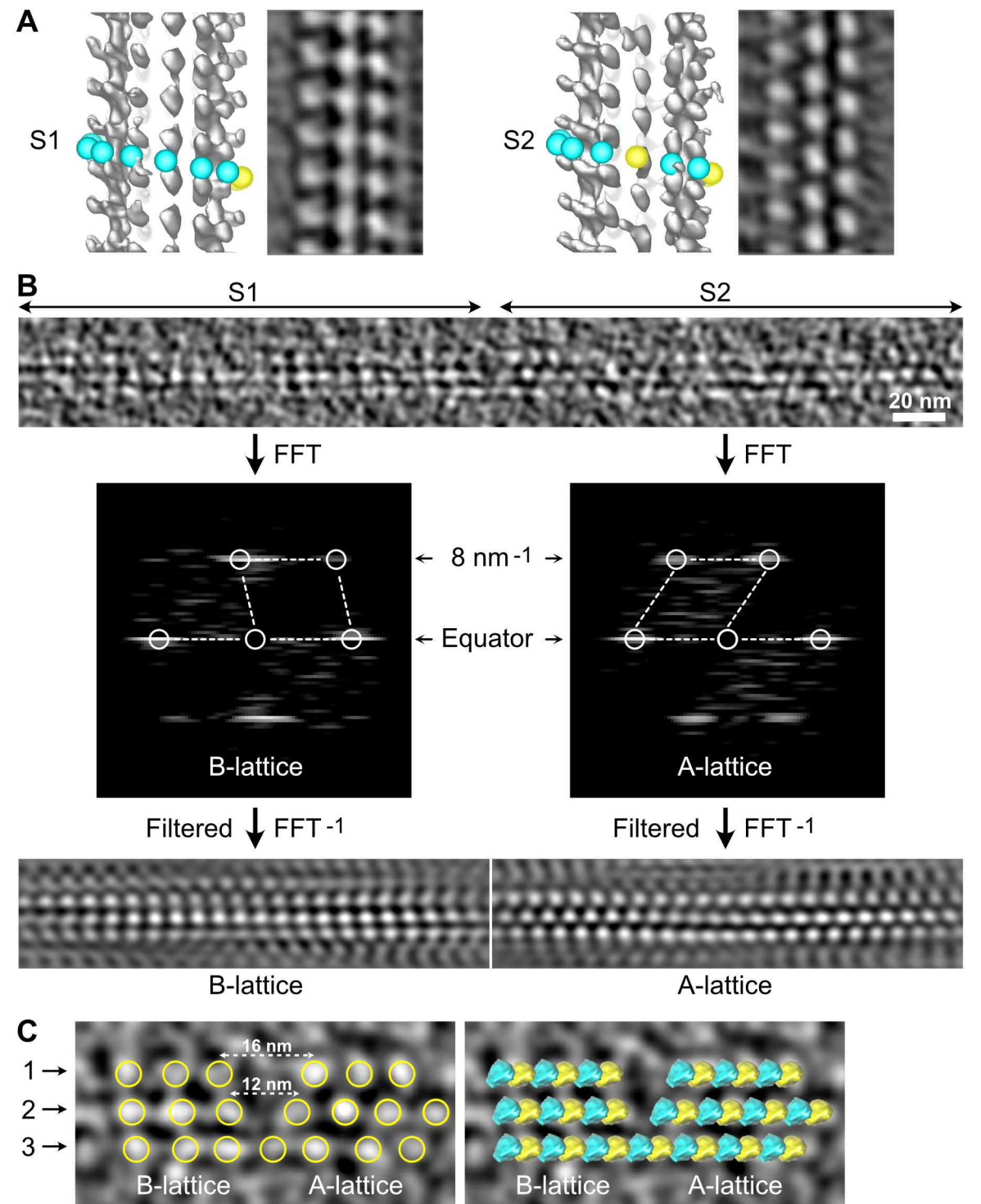
A
S1
S2
B
S1
S2
20 nm
FFT
FFT
8 nm -1
Equator
B-lattice
A-lattice
Filtered FFT -1
Filtered FFT -1
B-lattice
A-lattice
C
1
2
3
16 nm
12 nm
B-lattice
A-lattice
B-lattice
A-lattice

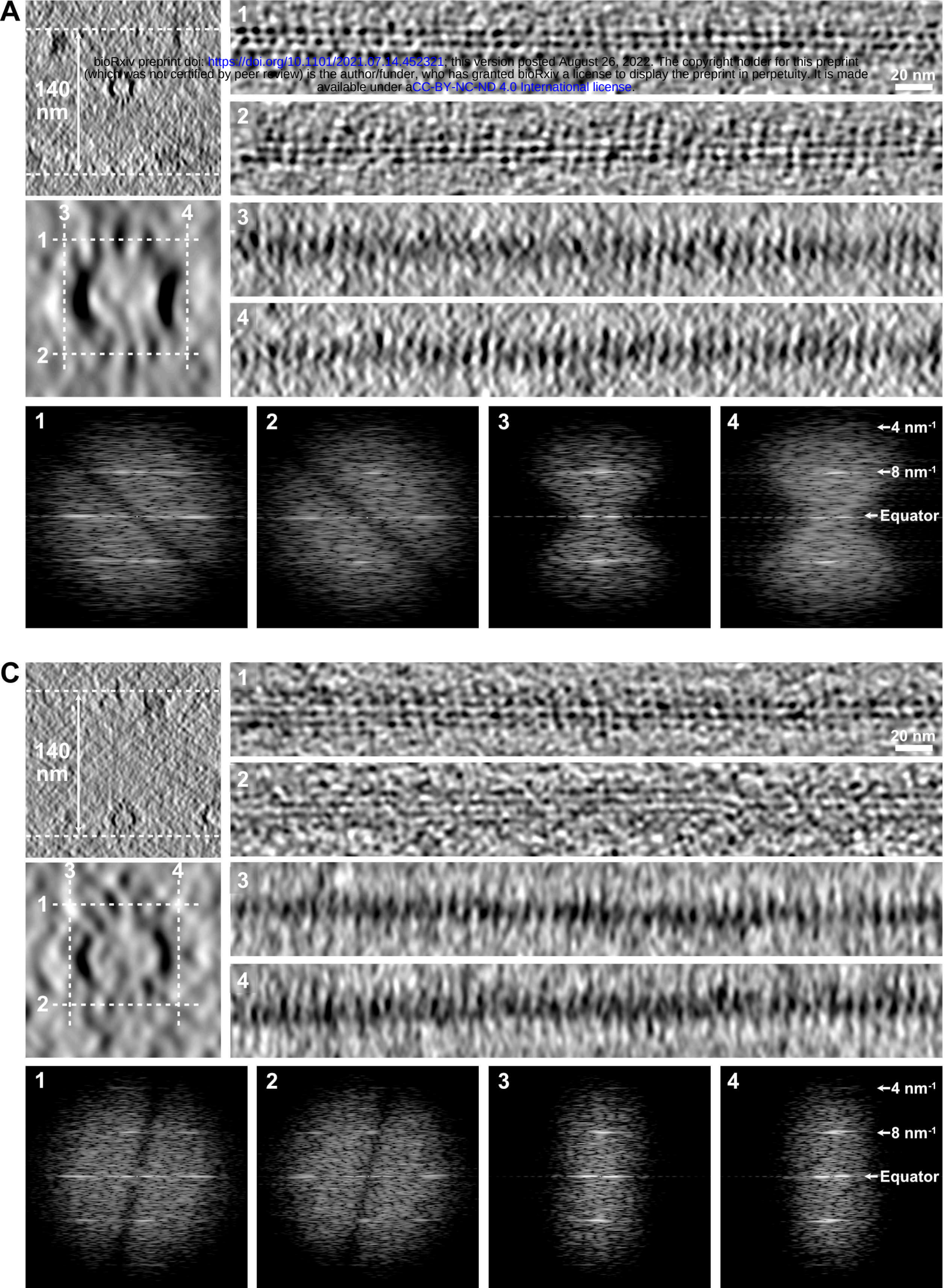

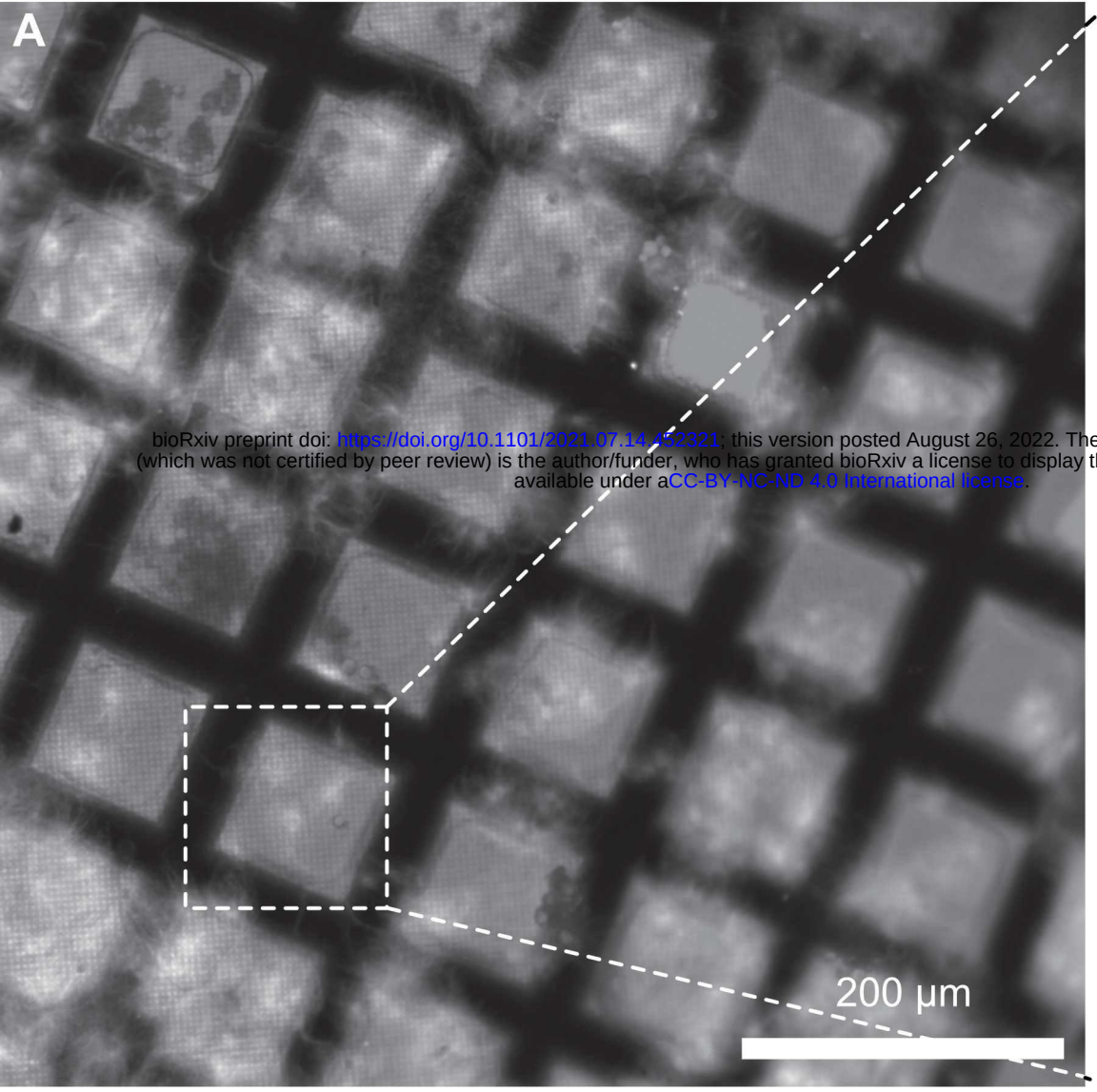

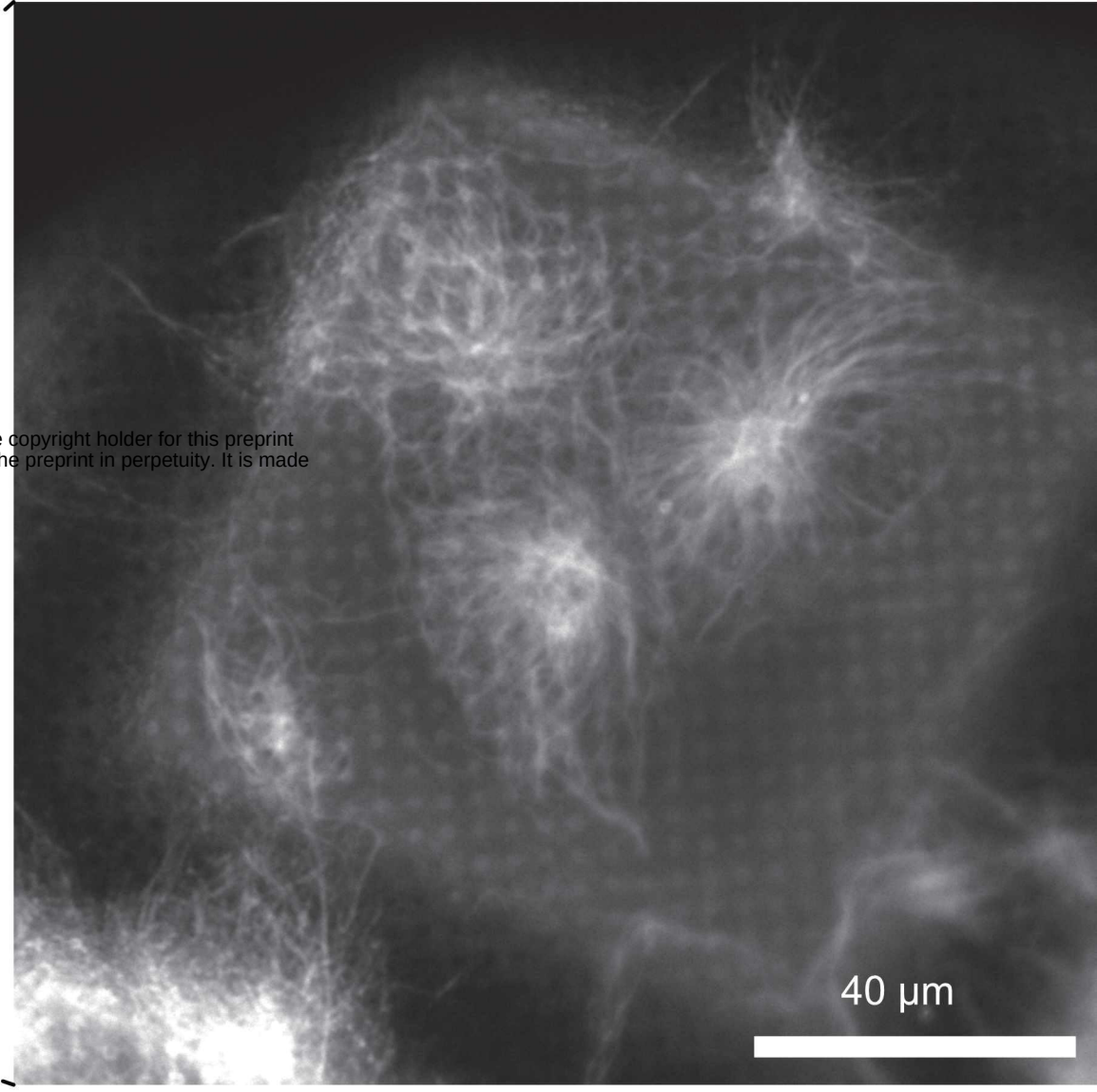

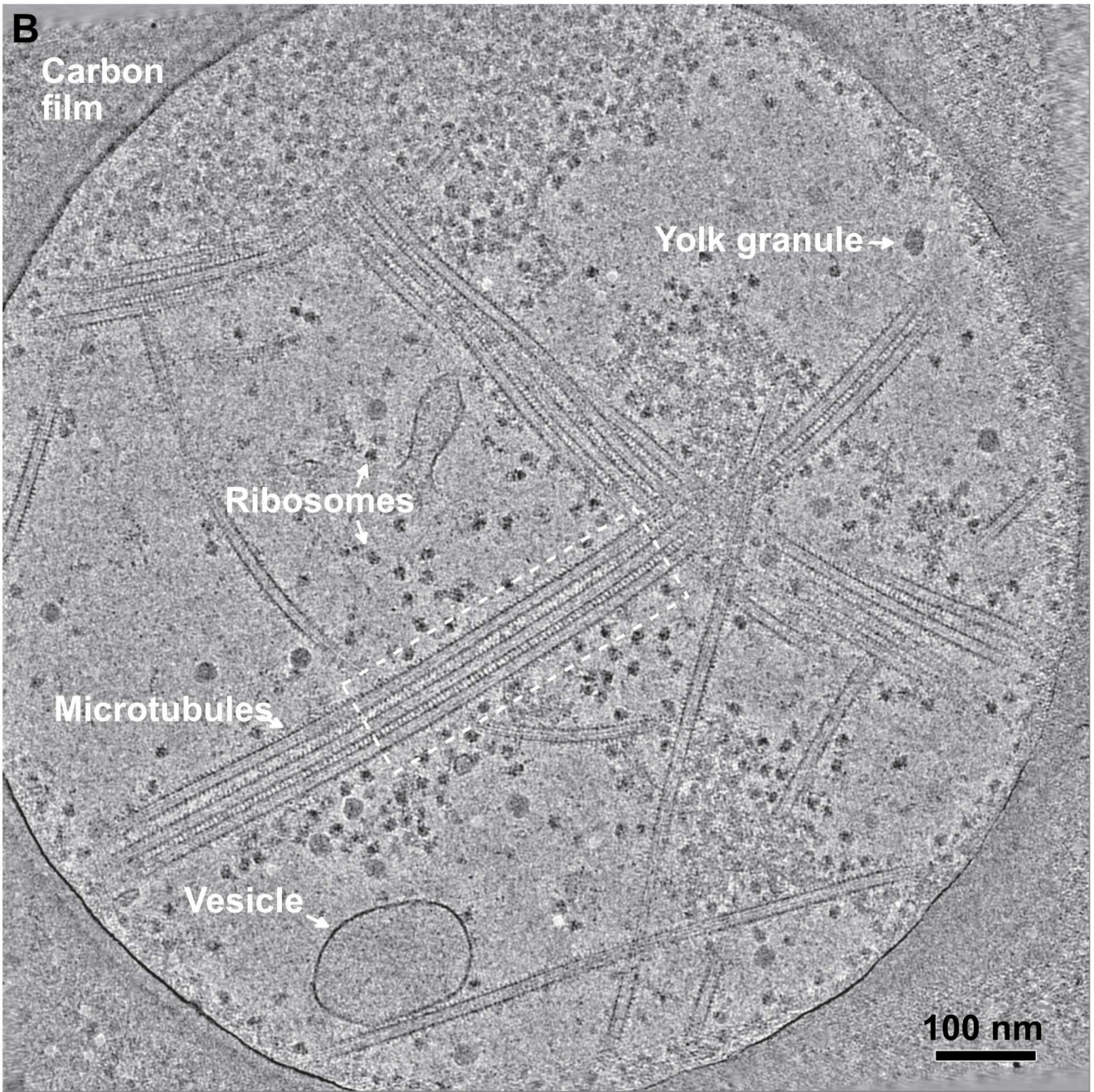

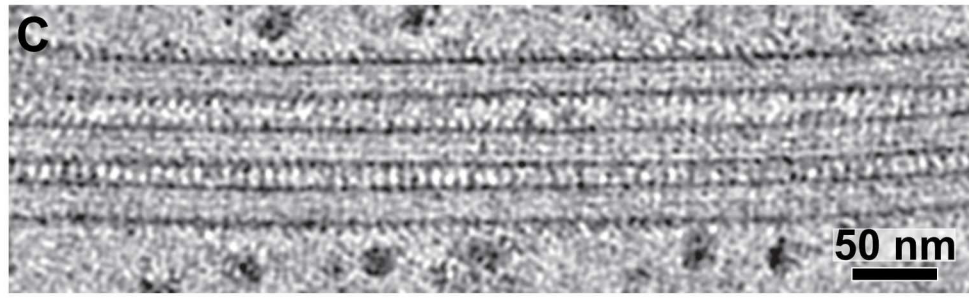

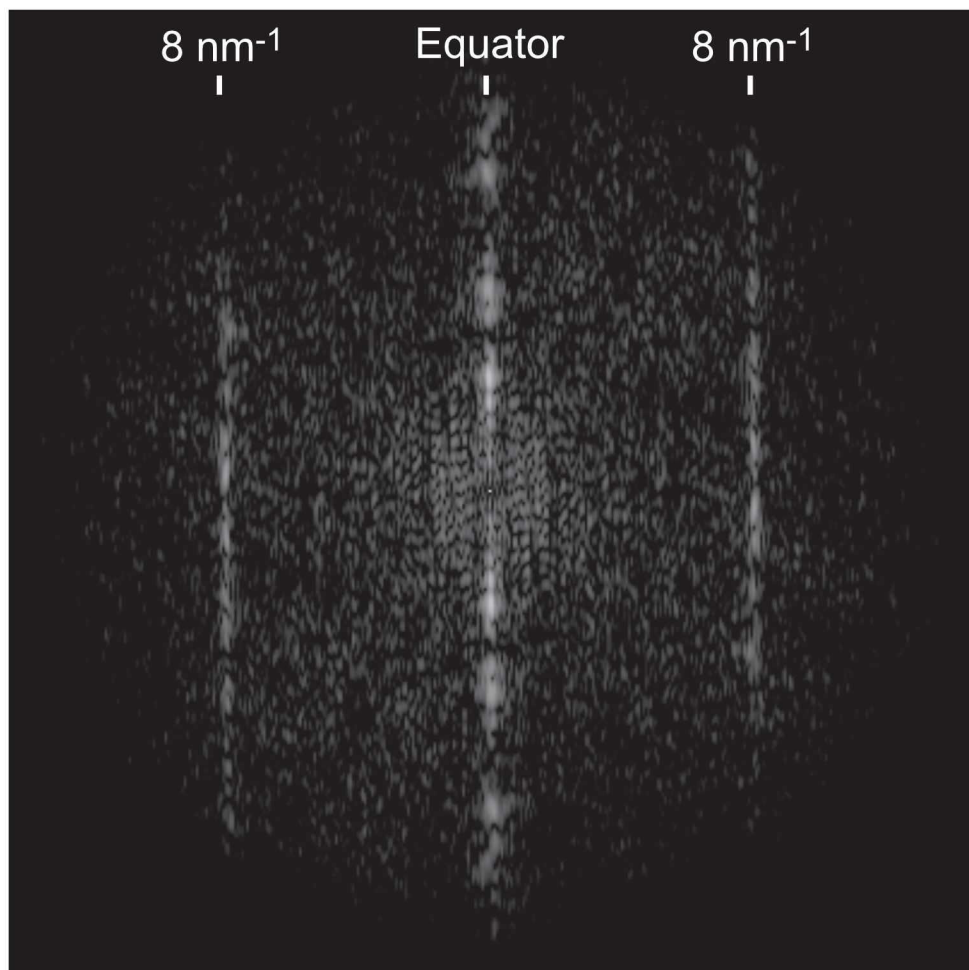

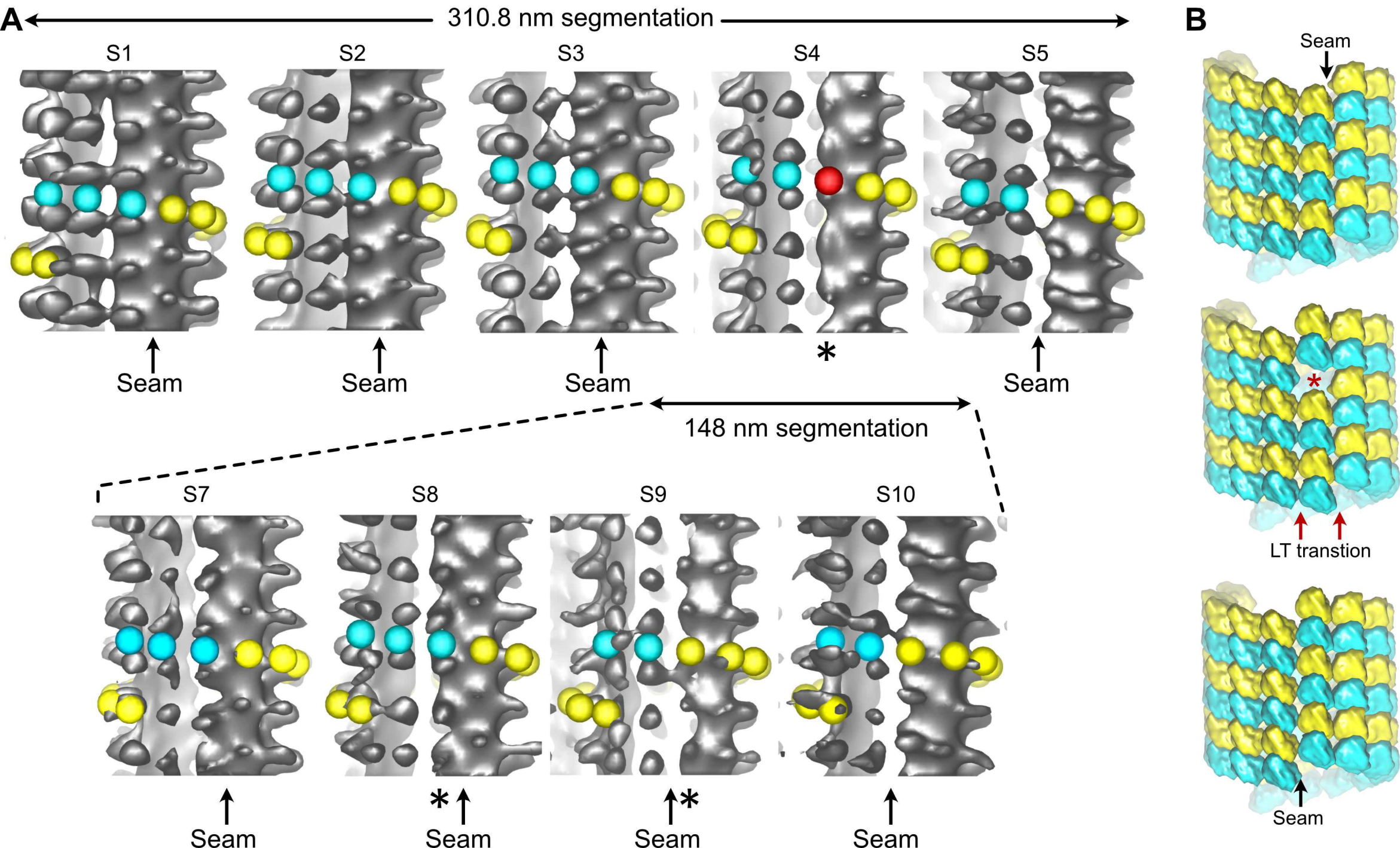
A
310.8 nm segmentation
S1
S2
S3
S4
S5
Seam
Seam
Seam
*
Seam
148 nm segmentation
S7
S8
S9
S10
Seam
* Seam
Seam *
Seam
B
Seam
*
LT transtion
Seam

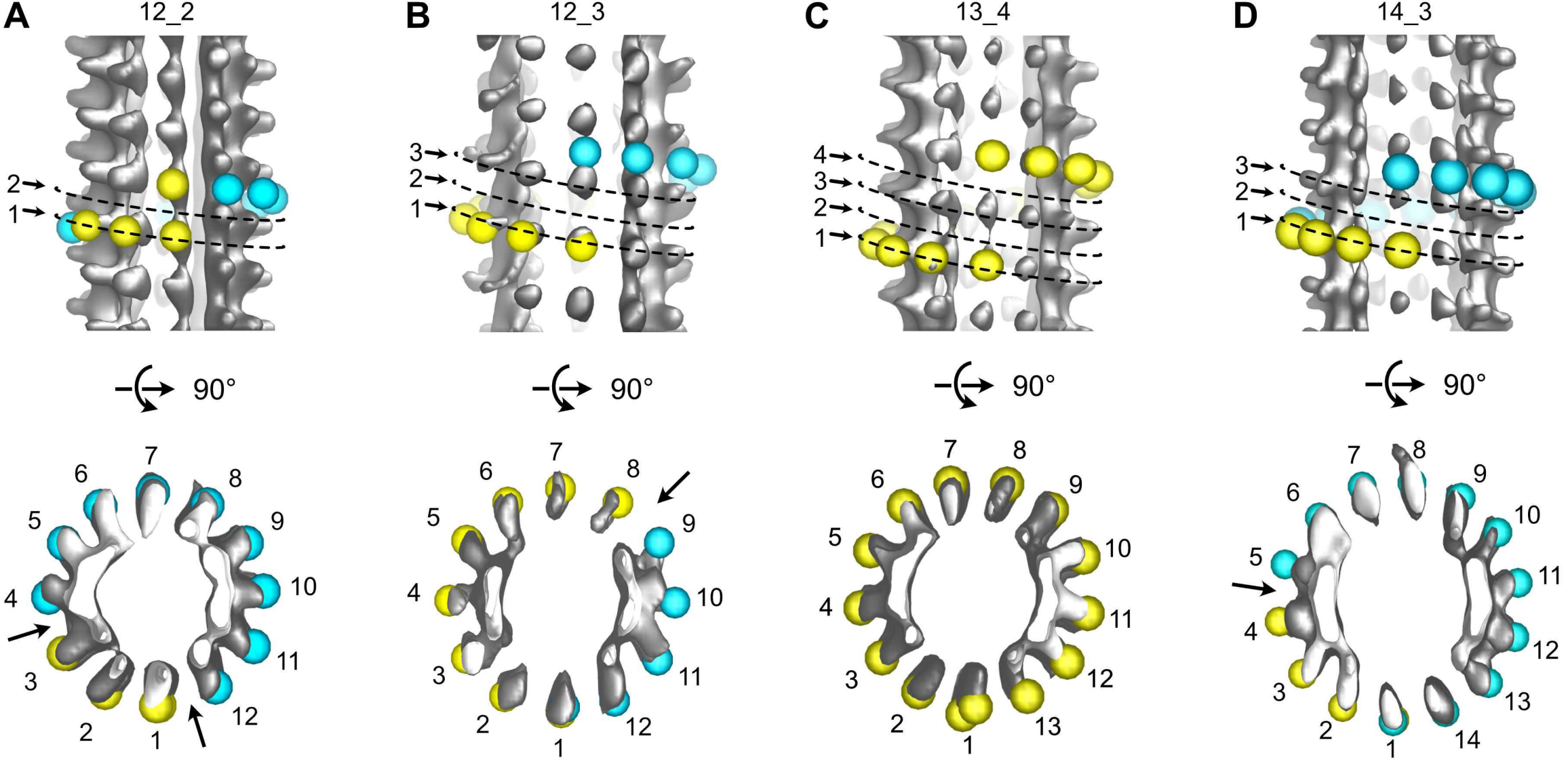
A
12_2
2
1
90°
7
6
8
5
9
4
10
3
11
2
1
12
B
12_3
3
2
1
90°
7
6
8
5
9
4
10
3
11
2
12
1
C
13_4
4
3
2
1
90°
7
8
6
9
5
10
4
11
3
12
2
13
1
D
14_3
3
2
1
90°
7
8
6
9
5
10
4
11
3
12
2
13
1
14